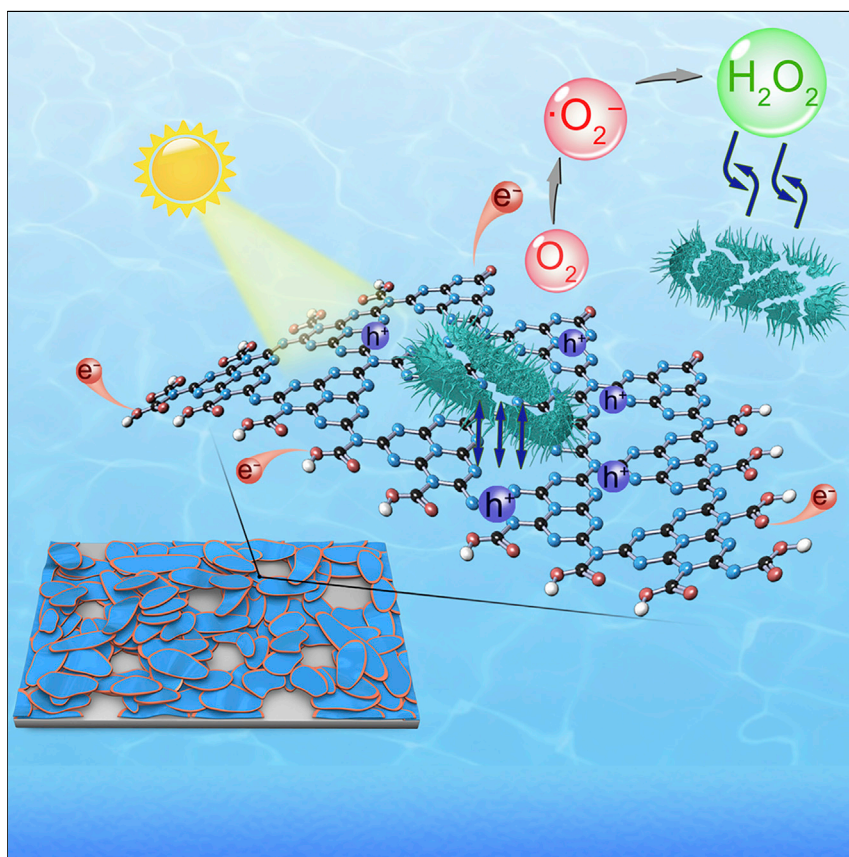


Article

Edge-Functionalized g-C₃N₄ Nanosheets as a Highly Efficient Metal-free Photocatalyst for Safe Drinking Water

The electron-withdrawing groups were selectively introduced onto the edge of g-C₃N₄ nanosheets. The edge functionalization not only induces an upward bending that improves the adsorption of oxygen molecules but also promotes the separation of photo-generated electron-hole pairs. By using these nanosheets as the photocatalyst for water disinfection, Dan Wang and colleagues achieved a record-high efficiency toward the photo-disinfection of *Escherichia coli* under visible-light irradiation among all metal-free catalysts.

Zhenyuan Teng, Nailiang Yang, Hongying Lv, ..., Chengyin Wang, Dan Wang, Guoxiu Wang

wangcy@yzu.edu.cn (C.W.)
danwang@ipe.ac.cn (D.W.)
guoxiu.wang@uts.edu.au (G.W.)

HIGHLIGHTS

Selectively functionalize electron-withdrawing groups on the edges of g-C₃N₄ nanosheets

A record-high disinfection efficiency toward *Escherichia coli*-rich water is obtained

The first-order disinfection rate is comparable with that of the best metal-based photocatalyst



Article

Edge-Functionalized g-C₃N₄ Nanosheets as a Highly Efficient Metal-free Photocatalyst for Safe Drinking Water

Zhenyuan Teng,^{1,6} Nailiang Yang,^{2,5,6} Hongying Lv,¹ Sicong Wang,¹ Maozhi Hu,⁴ Chengyin Wang,^{1,*} Dan Wang,^{2,5,7,*} and Guoxiu Wang^{1,3,*}

SUMMARY

Solar water disinfection catalyzed by metal-free photocatalyst has emerged as a promising approach for clean water production. By using the edge-functionalized graphitic carbon nitride (g-C₃N₄) as photocatalytic disinfectants, we find that the pathogen-rich water can be rapidly purified in 30 min with a disinfection efficiency of over 99.9999% under visible-light irradiation, which meets the requirement for drinking water. The edge-functionalized g-C₃N₄ shows a first-order disinfection rate that is five times higher than the previously reported best metal-free photocatalyst but only consumes 1/10 of the catalyst. The catalytic activity is also comparable to that of the best metal-based photocatalyst. Results of the highest occupied molecular orbitals and Mulliken charge distribution reveal that the exposed -COOH and C=O groups at the edges of g-C₃N₄ nanosheets not only significantly promote charge separation but also induce the upward bending of the surface band, facilitating the generation of hydrogen peroxide.

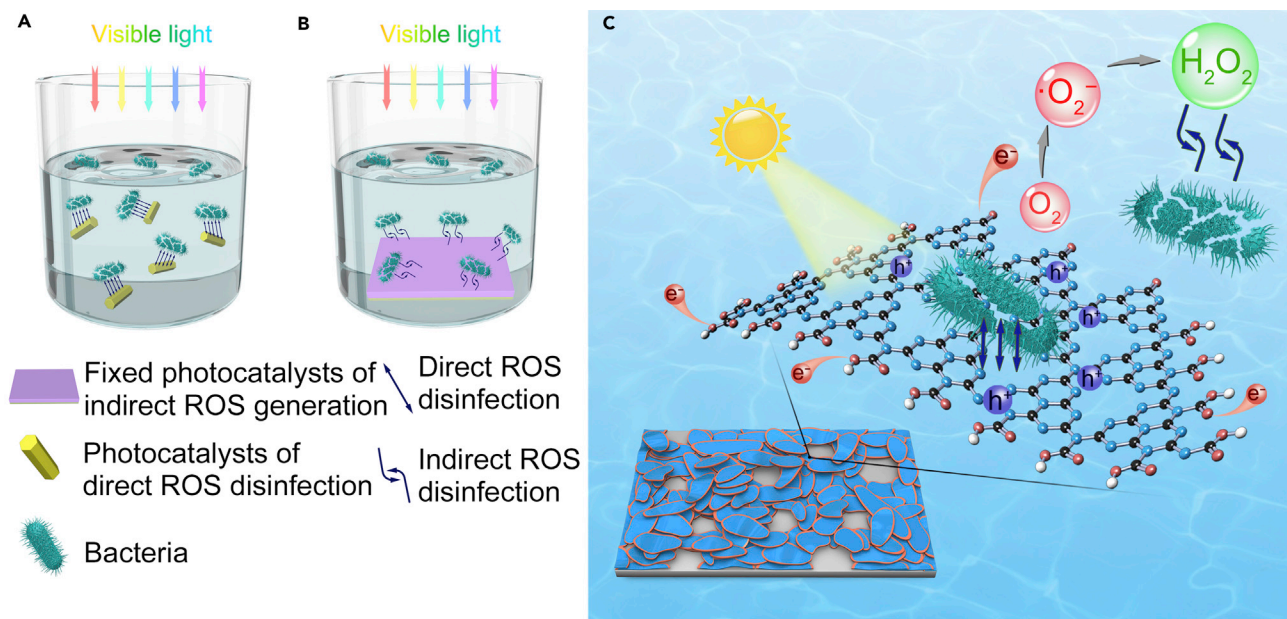
INTRODUCTION

The development of effective and energy-efficient water disinfection technologies is extremely urgent to relieve clean water scarcity and global energy shortage.^{1–5} Photocatalytic disinfection is considered to be a promising approach.^{6–9} Nowadays, the most efficient photocatalysts for disinfection are metal-based nanomaterials, but they are likely to cause secondary pollution because of the inevitable release of metal ions.^{10–16} Hence, it is of great importance to seek highly efficient metal-free photocatalysts for water disinfection. Until now, the efficiency of the reported metal-free photocatalysts has been much lower than that of metal-based photocatalysts. One of the reasons is that the surface of carbon materials is chemically inert and hydrophobic, which limits their application in catalysis, especially in aqueous solutions.^{17,18} Another reason is that the band gaps of the widely studied carbon materials—such as carbon nanotubes, graphene, and graphene oxide—are too small to effectively generate electron-hole pairs.^{19,20} Thus, they cannot produce enough reactive oxygen species (ROS) to inactivate pathogen via photocatalysis.

Recently, graphitic carbon nitride (g-C₃N₄), first reported by Wang et al.²¹ as a fascinating two-dimensional layered metal-free semiconductor with a band gap of approximately 2.7 eV, drew broad interdisciplinary attention for its photocatalytic abilities.^{22–30} Wang et al. also first reported the disinfection effect of g-C₃N₄.²² However, the photocatalytic disinfection efficiency of g-C₃N₄ is much lower than that of metal-based photocatalysts because of its fast recombination.^{23,24} Many approaches, such as element doping and morphology control, have been adopted

The Bigger Picture

Discovering highly efficient metal-free catalysts for photocatalytic disinfection will be greatly beneficial for the alleviation of the issues of clean water scarcity and global energy shortage. In addition, secondary pollution resulting from the use of metal-based catalysts can be avoided. In our work, we prepared the edge-functionalized g-C₃N₄ by selectively introducing electron-withdrawing groups at the edges of g-C₃N₄ nanosheets by using a facile wet-chemical method. Among all the metal-free photocatalysts currently used in the disinfection of model *Escherichia coli* under visible-light irradiation, this method reaches a record efficiency. Notably, this edge functionalization generates an anisotropic built-in electric field that promotes the separation of photo-generated electron-hole pairs. This work provides a new strategy for controlling surface charge density, which could lead to the discovery of additional unique properties and promising applications in catalysis, electronics, and targeted therapy.



Scheme 1. Disinfection Schematics of Different Photocatalysts

(A and B) Solar water disinfection mechanism of (A) direct ROS (such as h^+ , 1O_2) and (B) indirect ROS (such as $\cdot O_2^-$ and H_2O_2). (C) Schematic diagram of indirect bacteria inactivation using H_2O_2 generated by an edge-functionalized g-C₃N₄ nanosheet.

to improve the catalytic activity, but the limited enhancement achieved so far leaves it still far from feasible with respect to practical application,^{31–37} and the efficiency still remains inferior to that of metal-based catalysts.^{13–16,38–42} Considering that the introduction of electron-withdrawing groups can modify the charge distribution on nanomaterials,^{43–47} we propose a novel method to promote the charge separation efficiency of g-C₃N₄ by introducing electron-withdrawing groups at the edge of g-C₃N₄ nanosheets, which can induce an anisotropic built-in electric field in the two-dimensional plane, and thus the recombination can be suppressed.

Herein, we synthesized the edge-functionalized g-C₃N₄ nanosheets by using a facile method and investigated its photocatalytic disinfection performance (Scheme 1). Notably, a record-high efficiency of $-\log_{10}(C/C_0) = 6$ (>99.9999%) in the disinfection of model *Escherichia coli* (*E. coli*) was obtained in 30 min under visible-light irradiation. Meanwhile, its first-order disinfection rate is five times higher than that of previously reported best metal-free photocatalysts with only 1/10 catalyst consumption. This remarkably high efficiency is also comparable to that of the best metal-based photocatalysts. With further investigation using transmission electron microscopy (TEM), density functional theory (DFT) calculations, and electron spin resonance (ESR), it was found that the edge functionalization of g-C₃N₄ nanosheets not only induces an upward bending of their energy band, which improves the adsorption of oxygen molecules, but also promotes the separation of photo-generated electron-hole pairs. Importantly, this catalyst was also incorporated into portable devices for highly efficient and large-scale water disinfection, producing water that reaches the standard of drinking water. Thus, these devices are believed to be very promising for commercial applications.

RESULTS AND DISCUSSION

Preparation and Characterization of Functionalized g-C₃N₄ Nanosheets

Three kinds of functionalized g-C₃N₄ nanosheets with different oxidization degrees (g-C₃N₄-30, g-C₃N₄-45, and g-C₃N₄-60) were prepared by an improved Hummer's

¹College of Chemistry and Chemical Engineering, Yangzhou University, 180 Si-Wang-Ting Road, Yangzhou 225002, China

²State Key Laboratory of Biochemical Engineering, Institute of Process Engineering, Chinese Academy of Sciences, No. 1 Beiertiao, Zhongguancun, Beijing 100190, China

³Centre for Clean Energy Technology, University of Technology Sydney, City Campus, Broadway, Sydney, NSW 2007, Australia

⁴Test Center of Yangzhou University, Yangzhou University, 48 Wen-Hui-Dong Road, Yangzhou 225009, China

⁵University of Chinese Academy of Sciences, 19A Yuquan Road, Beijing 100049, China

⁶These authors contributed equally

⁷Lead Contact

*Correspondence: wangcy@yzu.edu.cn (C.W.), danwang@ipe.ac.cn (D.W.), guoxiu.wang@uts.edu.au (G.W.)

<https://doi.org/10.1016/j.chempr.2018.12.009>

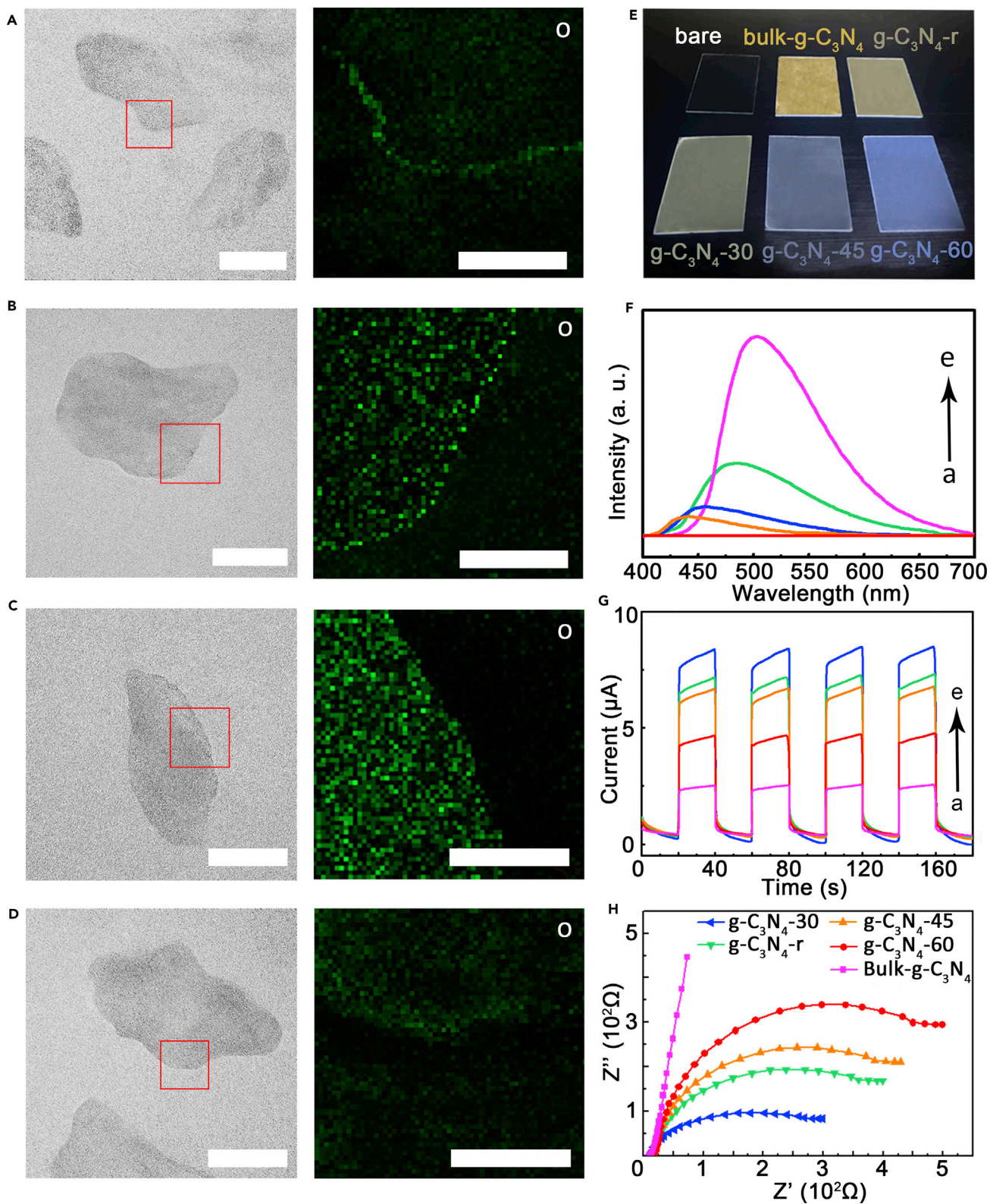


Figure 1. Morphologies and Photochemical Properties of Functionalized $g\text{-C}_3\text{N}_4$ Nanosheets with Different Oxidation Degrees

(A–D) TEM images and STEM-EDS mappings (oxygen distributions are presented) of (A) $g\text{-C}_3\text{N}_4\text{-30}$, (B) $g\text{-C}_3\text{N}_4\text{-45}$, (C) $g\text{-C}_3\text{N}_4\text{-60}$, and (D) $g\text{-C}_3\text{N}_4\text{-r}$. Each scale bar represents 100 nm.

Figure 1. Continued

(E) Optical image of the disinfection films prepared by drop casting 1.00 mL suspension containing various catalysts (0.50 mg/mL) onto 2.0 × 2.5 cm² glass substrate.

(F) Photoluminescence (PL) spectra of carbon nitride samples obtained by irradiation at a wavelength of 410 nm (a, g-C₃N₄-60; b, g-C₃N₄-45; c, g-C₃N₄-30; d, g-C₃N₄-r; e, bulk-g-C₃N₄).

(G) Photocurrent spectra of different films prepared with various samples (a, bulk-g-C₃N₄; b, g-C₃N₄-60; c, g-C₃N₄-45; d, g-C₃N₄-r; e, g-C₃N₄-30; the area of the film is 1 cm².) under vis + IR irradiation.

(H) EIS obtained by measuring these g-C₃N₄ samples under vis + IR irradiation.

method with different oxidization durations (30, 45, and 60 min, respectively). G-C₃N₄-r was also obtained by reducing g-C₃N₄-60 with NH₂NH₂·H₂O.⁴⁸ TEM images show that the morphologies of these four samples are quite similar, whereas scanning TEM-energy-dispersive X-ray spectroscopy (STEM-EDS) mappings show that their oxygen distributions are significantly different (Figures 1A–1D). It was found that after oxidization for 30 min, the concentration of oxygen at the edges was higher than that on the surface (g-C₃N₄-30; Figure 1A). With the elongated oxidization duration, the concentration of the oxygen on the surface gradually increased, resulting in a more homogeneous distribution of oxygen from the edge to the surface of g-C₃N₄ nanosheets (Figures 1B and 1C). As for the distribution of carbon and nitrogen, there was no obvious difference among these four samples (Figure S1).

Generally, photocatalytic performance is greatly influenced by two factors: (1) the number of photons absorbed by the material and (2) the separation efficiency of the photo-generated electron-hole pairs.¹⁴ As shown in Figure 1E, the films fabricated by various photocatalysts (denoted as F-g-C₃N₄, including F-bulk-g-C₃N₄, F-g-C₃N₄-r, F-g-C₃N₄-30, F-g-C₃N₄-45, and F-g-C₃N₄-60) presented different colors from yellow to white, indicating that the band-gap width increases with increasing degrees of oxidation. Together with the results of ultraviolet diffuse reflectance spectra (UV-DRS), XPS measurement, and the Mott-Schottky test (Figure S2), the position of the conduction band gradually shifted upward when the oxidization degree was increased. The band potentials of these samples are presented in Figure S3. Although the smallest band gap was found in bulk-g-C₃N₄, its highest fluorescence response indicates the easiest recombination of photo-excited electron-hole pairs, which releases energy as light (Figure 1F) and is not desirable for photocatalysis. On the other hand, the material with the highest oxidation degree, i.e., g-C₃N₄-60, showed the lowest recombination of photo-excited electron-hole pairs from the photoluminescence spectra (Figure 1F), but its largest band gap limited light utilization, which is also not desirable for photocatalysis.

Photocurrent measurements (Figure 1G) and electrochemical impedance spectroscopy (EIS) (Figure 1H) both showed that g-C₃N₄-30 exhibited the lowest electron-transfer resistance under visible-light irradiation. Results of high-resolution XPS revealed that the concentration of –COOH and C=O in g-C₃N₄-30, g-C₃N₄-45, and g-C₃N₄-60 stayed almost constant (Figure S4; Table S1). The increased degrees of oxidization exhibited in these materials are attributed to the further functionalization of hydroxyl groups (–OH) (Table S1). The –OH groups on g-C₃N₄ nanosheets hindered the in-plane electron transfer under the irradiation of visible light because the integrality of the delocalized π-conjugated bond might be partially reduced. On the other hand, the oxygen-functionalized groups were almost removed after reduction of hydrazine hydrate (HHA), i.e., g-C₃N₄-r; however, we also found that the photocurrent of the g-C₃N₄-30 was significantly higher than that of g-C₃N₄-r, and g-C₃N₄-r showed a higher charge-transfer resistance than

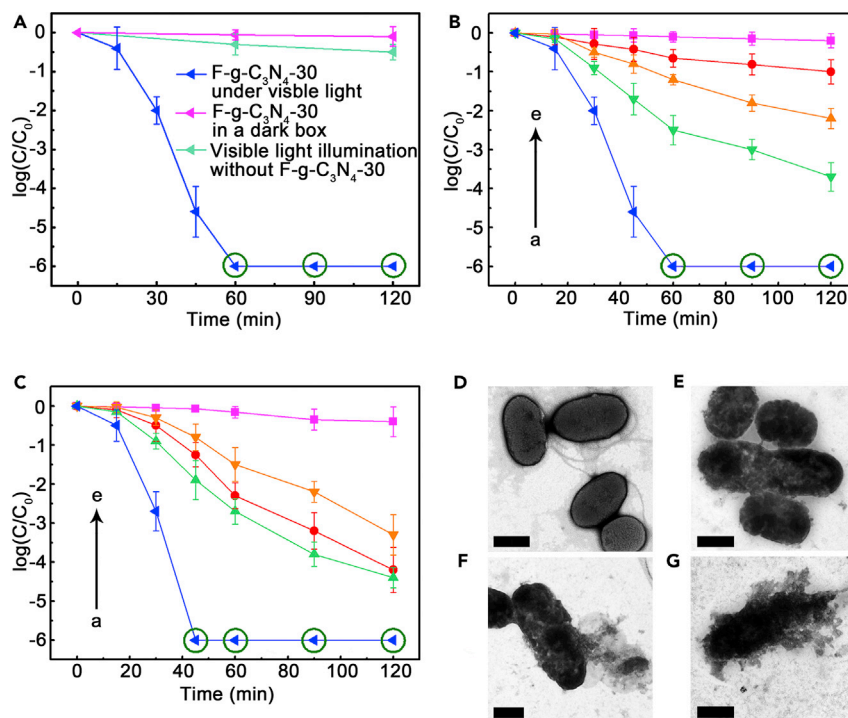


Figure 2. Disinfection Performance of F-g-C₃N₄

(A) Comparison of the disinfection performances of F-g-C₃N₄-30 with control experiments. (B and C) The disinfection performances of films of different g-C₃N₄ samples under (B) vis + IR irradiation and (C) full-spectrum solar-light irradiation (a, F-g-C₃N₄-30; b, g-C₃N₄-r; c, F-g-C₃N₄-45; d, F-g-C₃N₄-60; e, bulk-g-C₃N₄). (D–G) TEM images of *E. coli* (with F-g-C₃N₄-30 as the photocatalyst) (D) before and after irradiation for (E) 15 min, (F) 30 min, and (G) 45 min. Each scale bar represents 500 nm. In the disinfection performance curves, the error bars represent the standard deviations of five replicate measurements, and the data point with a dark green circle means that no live bacterium was detected.

g-C₃N₄-30. In this case, considering its efficient light utilization, slow charge recombination, and the lowest electron-transfer resistance, g-C₃N₄-30, with its edge functionalized by –COOH, might achieve the highest photocatalytic activity among these materials.

Photocatalytic Disinfection Performance of F-g-C₃N₄-30

By optimizing the coating mass of g-C₃N₄-30, the catalyst consumption was set to be 0.50 mg on a 5.0 cm² substrate for 50 mL of contaminated water (Figure S5). Unless otherwise stated, for a typical experiment, photocatalytic disinfection performance was tested with F-g-C₃N₄-30 as the photocatalyst and *E. coli* as a process indicator in the following experiments.

F-g-C₃N₄-30 showed an efficiency over 99.9999% under irradiation by a xenon lamp with a long-pass filter (visible and infrared [vis + IR] irradiation, λ > 400 nm) for 60 min, and the first-order disinfection rate (*k*) was 0.068 min^{−1} (R² = 0.91). In the control experiments (without F-g-C₃N₄-30 or light), the disinfection efficiency was below 50% under the same conditions (Figure 2A). Furthermore, F-g-C₃N₄-30 showed the highest disinfection efficiency among all the F-g-C₃N₄ samples with the same mass loading under the same experimental conditions (Figure 2B). Meanwhile, F-g-C₃N₄-30 also exhibited excellent disinfection performances for the inactivation of gram-negative bacterium (*Salmonella*)

and gram-positive bacterium (*Enterococcus faecalis*). No live bacteria were detected after vis + IR irradiation for 60 min (Figure S6A).

The disinfection performances of all types of g-C₃N₄ films were further tested with xenon lamps without any filters to simulate the solar light irradiation. Figure 2C shows that the g-C₃N₄ films exhibited better performance under irradiation with the full solar spectrum than under the aforementioned condition, i.e., using only vis + IR irradiation. F-g-C₃N₄-30 achieved a remarkably high activity in inactivating bacteria with an inactivation efficiency of $-\log_{10}(C/C_0) = 6$ (equivalent to >99.9999%) and a first-order disinfection rate (k) of 0.081 min^{-1} ($R^2 = 0.90$). When sunlight was used as the light source with an irradiation intensity of 102.23 mW/cm^2 , the cell walls and membranes of *E. coli* were gradually destroyed, and no living bacteria could be detected after 45 min of irradiation using F-g-C₃N₄-30 as the catalyst (Figures 2D–2G, S7, and S8). The destruction of cell walls and membranes indicates the critical role of the photo-generated ROS in the disinfection process.³³

To further investigate the photo-thermal effect of IR light on the disinfection performance, we also measured the disinfection efficiencies of *E. coli* in aqueous solution by using F-g-C₃N₄-30 as the catalyst under the illumination of a xenon lamp with a red-pass filter, i.e., only IR irradiation (Figure S9). The disinfection efficiencies are shown in Figure S10. The pure IR irradiation brought a much lower disinfection efficiency (25%) than did vis + IR irradiation (>99.9999%). Additionally, a temperature-control test further eliminated the thermal effect (Figure S11). Therefore, visible-light photocatalysis, rather than the photo-thermal effect, was proven to be responsible for the disinfection.

Finally, the stability of F-g-C₃N₄-30 was also investigated. The photocatalytic disinfection performance of F-g-C₃N₄-30 showed no obvious decline after 40 cycles (Figure S12). Additionally, the chemical state of the elements in g-C₃N₄-30 and the crystal structure of g-C₃N₄-30 showed no obvious change after a long period of disinfection (60 hr) (Figures S13 and S14). Therefore, F-g-C₃N₄-30 is stable during the photocatalytic disinfection process.

Disinfection Mechanism

During the solar water disinfection, ROS inactivated pathogens by their oxidation. We define ROS in aqueous solution as direct ROS ($\cdot\text{OH}$, $^1\text{O}_2$, and $\cdot\text{O}_2^-$; Scheme 1A) or indirect ROS (H_2O_2 , Scheme 1B) on the basis of the disinfection mechanism. To identify the mechanism, we measured the ROS in all F-g-C₃N₄ disinfection systems and detected four types of ROS ($\cdot\text{O}_2^-$, $^1\text{O}_2$, H_2O_2 , and $\cdot\text{OH}$) (Figure S15).^{49–55} The related scavenger-quenching experiments indicated that H_2O_2 plays the most important role in bacterial inactivation among all the ROS (Figure S16). Compared with the extremely short lifetime of photo-generated h^+ (at the ps or ns level),^{49,50} H_2O_2 has a much longer lifetime (1–2 days) in aqueous solution.^{51,52} Because the diffusion distance of species for disinfection in aqueous solution is relevant to their lifetime,^{53–55} h^+ is more difficult to diffuse than H_2O_2 . Thus, close interactions (or direct contact) between bacteria and photocatalysts is crucial for acquiring high activity when h^+ serves as the main disinfectant. Because g-C₃N₄-30 is fixed to the substrate, the photo-generated holes have much less possibility of directly contacting with bacteria than most of the previously reported photocatalysts dispersed in the bacterial suspension.^{33–37} To further confirm this speculation, we designed a control experiment to investigate the scavenging effects of h^+ (Figure S17), and we could conclude that H_2O_2 always serves as the most important disinfectant. Moreover, because the valence band position of g-C₃N₄-30 (1.58 V versus NHE, pH = 7) is

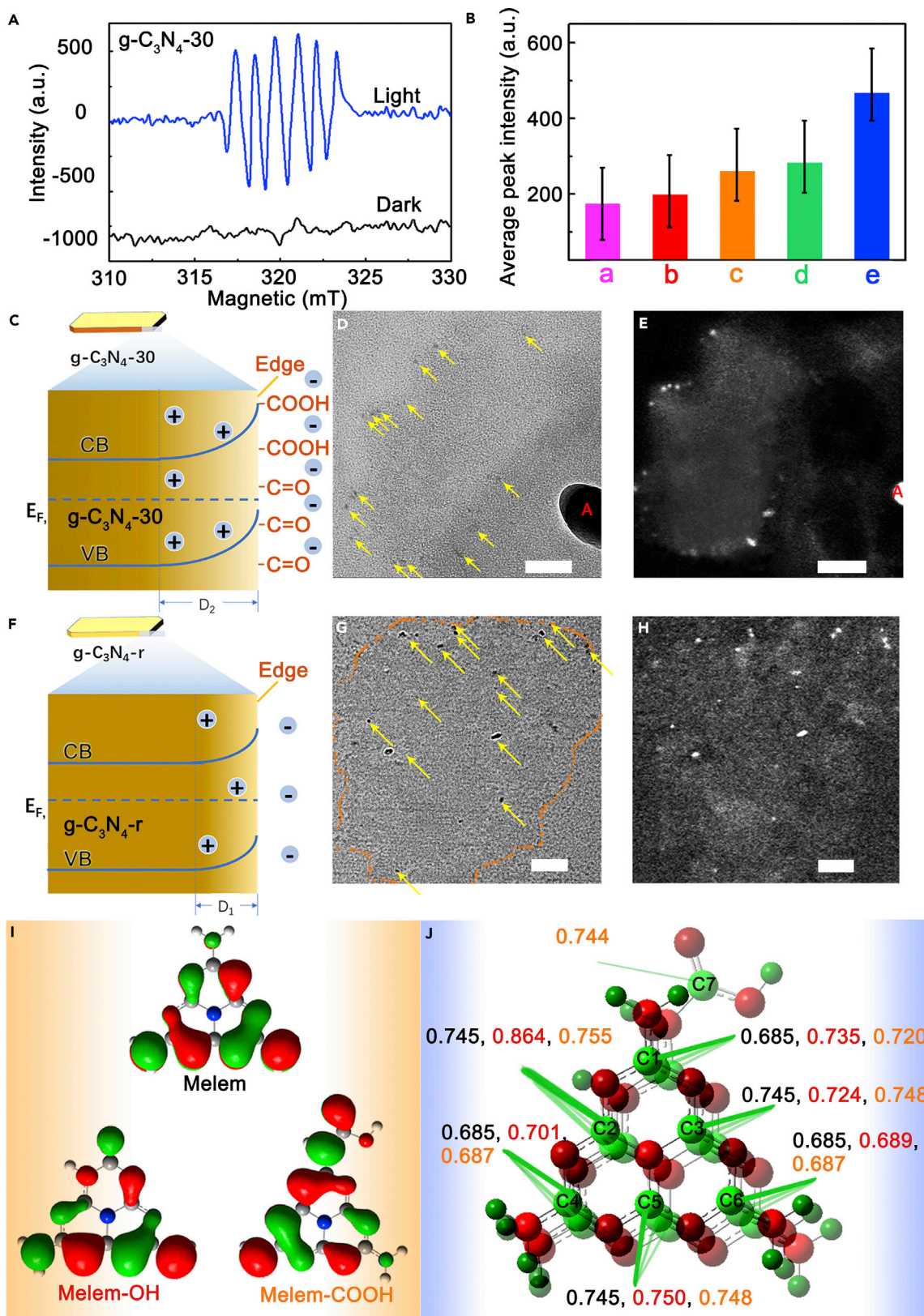


Figure 3. Verification of the Photocatalytic Disinfection Mechanism

(A) ESR spectrum of g-C₃N₄-30 in methanol solution using 5,5-dimethyl-1-pyrroline N-oxide as a radical trapper.
 (B) Average ESR signals of five kinds of photocatalytic disinfectants (a, bulk-g-C₃N₄; b, g-C₃N₄-60; c, g-C₃N₄-45; d, g-C₃N₄-r; e, g-C₃N₄-30). Error bars indicate the standard deviation of the absolute value of intensities of six characteristic peaks.
 (C–H) Schematic diagram of possible depletion layer and the band-bending effects near the edge of (C) g-C₃N₄-30 and (F) g-C₃N₄-r. Shown are TEM images of (D) g-C₃N₄-30 and (G) g-C₃N₄-r after photo-deposition of Pt nanoparticles (the yellow dotted line indicates the edge positions of g-C₃N₄-r) and high-angle annular dark field (HAADF) images of g-C₃N₄-30 (E) and g-C₃N₄-r (H) after photo-deposition of Pt nanoparticles. Each scale bar represents 50 nm in (D), (E), (G), and (H). Point A is the burning trace of the electron beam during HAADF measurement.
 (I) Highest occupied molecular orbitals of M_{elem}⁺, M_{elem}-OH⁺, and M_{elem}-COOH⁺.
 (J) Mulliken charge distribution of different carbon atoms in M_{elem}⁺ (black numbers), M_{elem}-OH⁺ (red numbers), and M_{elem}-COOH⁺ (orange numbers).

more negative than the redox potential of ·OH/OH⁻ (1.99 V versus NHE, pH = 7),^{22,52} OH⁻ can hardly be oxidized by the hole to generate ·OH. Therefore, it is not ·OH but H₂O₂ (Figures S16 and S17) that behaves as the major ROS for bacterial inactivation because of the dispersed state and band structure of g-C₃N₄-30.

F-g-C₃N₄-30 has shown its advantages in H₂O₂ generation among all samples (Figure S15D), and as known, H₂O₂ serves as a crucial disinfectant for achieving highly efficient indirect bacterial inactivation.¹⁴ To further understand the H₂O₂ generation mechanism, we performed electron spin resonance (ESR) measurements by using 5,5-dimethyl-1-pyrroline N-oxide (DMPO) as a trapping agent. Six characteristic peaks of DMPO·O₂⁻ were detected, indicating the generation of ·O₂⁻ with F-g-C₃N₄ as the photocatalyst under vis + IR irradiation (Figures S18 and 3A).³¹ As reported, ·O₂⁻ is a crucial active intermediate in the production process of H₂O₂; thus, the more ·O₂⁻ is generated, the more H₂O₂ will be produced. g-C₃N₄-30 showed the strongest signal of ·O₂⁻ among these catalysts (Figure 3B), indicating the highest amount of H₂O₂ generation.

Furthermore, at the molecular level, the high catalytic activity can be understood in detail from the following two aspects: band bending and charge separation.

Band Bending

In bulk semiconductors, charge transfer is isotropic.⁴⁷ In contrast, in the two-dimensional graphitic carbon nitride nanosheets, the charge transfer is anisotropic as a result of the sp² π-conjugation in a typical polymeric covalent semiconductor.²³ The transfer of photo-generated charges is confined in the two-dimensional plane, which results in different electric charge densities between marginal areas and central areas. Because g-C₃N₄ is an n-type semiconductor, a depletion layer may exist near the edge of g-C₃N₄ nanosheets (Figure 3F).⁴⁷ The edge functionalized by carboxyl and carbonyl groups will accumulate negative charges and then increase the thickness of the space-charge region (Figure 3C), which can result in an enhancement of upward band bending and significantly enhance separation efficiency of photo-generated electron-hole pairs.⁴⁷

Previous studies have shown that the photo-deposition of noble metal can prove the effects of edge functionalized -COOH and C=O groups in charge transfer and band bending.^{57,58} When the light radiates on the nanosheets, electrons are generated. The functional groups at the edges of g-C₃N₄-30 withdraw the electrons to the edge region, which enhances the separation of photo-generated electron and hole pairs. Accompanying the band bending, the reduction ability is enhanced;⁵⁷ thus, H₂PtCl₆ was reduced to Pt nanoparticles at the electron-rich domains, i.e., Pt nanoparticles were selectively deposited onto the edge region (Figures 3D and 3E).

In comparison, when we deposited Pt on g-C₃N₄-r by using the same method, the Pt nanoparticles were deposited at both edge and surface domains of g-C₃N₄-r (Figures

3G and 3H), which indicates that the photo-generated electrons were not withdrawn to the edge region of g-C₃N₄-r because there is little -COOH and C=O at the edges of g-C₃N₄-r (Figure S4). Therefore, a promoted charge transfer and band bending at the edge region of g-C₃N₄-30 exist because of the selective functionalization with -COOH and C=O, which can increase the chemisorption of oxygen molecules⁵⁶ so that the ESR signals of DMPO-·O₂⁻ are increased (Figure 3A) during the reduction process.

Charge Separation

DFT calculations proved that the functional groups at the edge can enhance the charge separation efficiency. To simulate the photo-generated positive charges near the edge of the g-C₃N₄-30, we set the charge number of the molecular models as +1. M_{elem}⁺ is used to represent the elementary unit of g-C₃N₄ (Figure 3I). Then, a carbonyl and a carboxyl are attached onto the edge of M_{elem} (denoted as M_{elem}-OH⁺ and M_{elem}-COOH⁺, respectively).⁵⁹ The DFT results reveal that carbonyls and carboxyls alter the orbital status of neighboring carbon atoms. The probability density of electrons on some neighboring carbon atoms is decreased, whereas the probability density of electrons on the oxygen atoms is significantly increased. Mulliken charge distributions of different carbon atoms at M_{elem}⁺, M_{elem}-OH⁺, and M_{elem}-COOH⁺ were also investigated. Figures 3J and S19 show that the positive charges on the carbon of M_{elem}-OH⁺ (C1, 0.735; C2, 0.864; C4, 0.701) and M_{elem}-COOH⁺ (C1, 0.720; C2, 0.755; C4, 0.687) are relatively higher than those on M_{elem}⁺ (C1, 0.685; C2, 0.745; C4, 0.685), which is attributed to the strong electron-accepting capability of carbonyls and carboxyls.⁶⁰ In addition, the positive charges of the carbon atoms at the edge (M_{elem}-OH⁺ C1, 0.735; M_{elem}-COOH⁺ C1, 0.720) are much higher than those away from the edges (M_{elem}-OH⁺ C4, 0.701, and C6, 0.689; M_{elem}-COOH⁺ C4, 0.687, and C6, 0.687). This makes the photo-excited electrons tend to aggregate at the edge of nanosheets, thus enhancing the charge separation, whereas the functionalization taken on the surface does not result in enhanced charge separation.

The efficient adsorption between bacteria and catalysts can also enhance the catalytic activity, but in our case, the isoelectric points (IEPs) of bulk-g-C₃N₄, g-C₃N₄-r, and g-C₃N₄-30 were measured to be 5.1, 6.1, and 5.8, respectively (Figure S20), indicating that the surfaces of the materials are all negative under the experimental condition (neutral aqueous solutions), and the surface of the bacteria is also negative under the experimental condition (IEPs of bacteria are between 2 and 5).⁶¹ Herein, the efficiency of the adsorption between bacteria and catalysts should be low because the charges on their surfaces are the same.⁶²

Device Fabrication

We can predict that increasing the exposure of carboxyl and carbonyl groups at the edge can further enhance catalytic activity. In this case, we adjusted the recipe for film preparation to enhance the exposure of the oxygen-rich group (denoted as F-g-C₃N₄-30-EP, 10 mg g-C₃N₄-30 on 5 cm² glass; Figures S21–S24). As shown in Figures 4A and 4B, F-g-C₃N₄-30-EP is more hydrophilic than F-g-C₃N₄-30, indicating that more oxygen atoms are exposed by this modified method. When a xenon lamp is used with a UV filter as the light source, the disinfection rate of F-g-C₃N₄-30-EP ($k = 0.14 \text{ min}^{-1}$, $R^2 = 0.98$) is twice as high as that of F-g-C₃N₄-30 ($k = 0.068 \text{ min}^{-1}$, $R^2 = 0.91$) and has a $-\log_{10}(C/C_0) \geq 6$ (>99.9999%) in 30 min (Figure 4C). Detailed discussions on the generation rate of ROS, the scavenger-quenching experiments, and the results of repeatability with F-g-C₃N₄-30-EP are shown in Figures S25–S27 and Supplemental Information Section 2.1. These results imply that effective exposure of carboxyl and carbonyl groups is capable of further facilitating H₂O₂ production for higher disinfection efficiency.

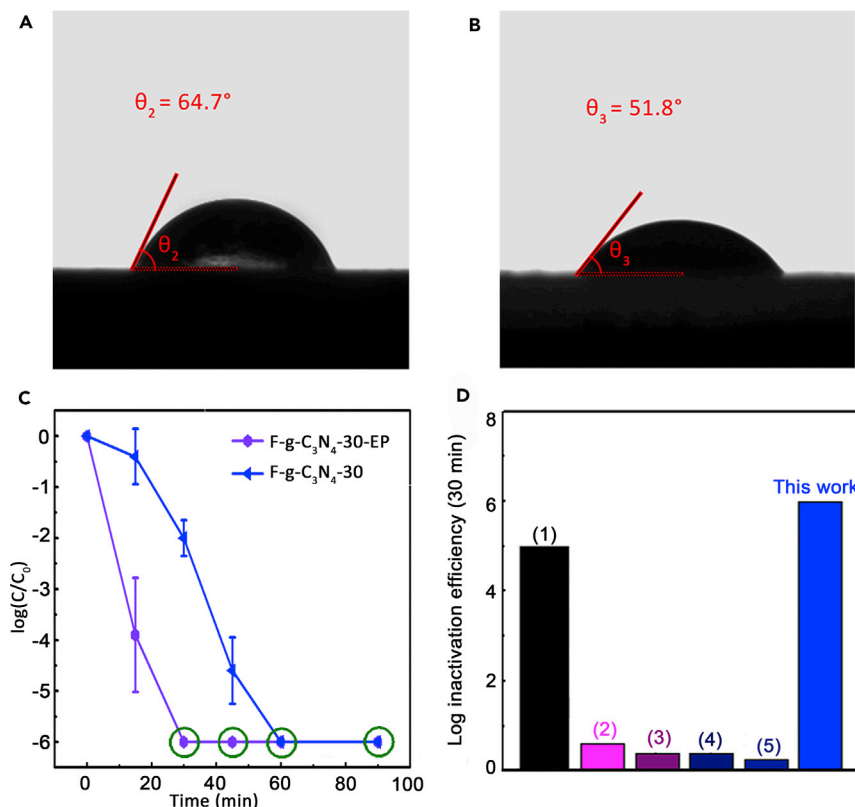


Figure 4. Improved Disinfection Performance with F-g-C₃N₄-30-EP as the Catalyst

(A and B) Contact-angle measurement of the film formed on glass by (A) F-g-C₃N₄-30 and (B) F-g-C₃N₄-30-EP.

(C) Comparison of disinfection efficiencies of F-g-C₃N₄-30 and F-g-C₃N₄-30-EP. Error bars represent the standard deviations of five replicate measurements, and data points with dark-green circles mean that no live bacterium was detected.

(D) Comparison of log disinfection efficiency (at time point of 30 min) of F-g-C₃N₄-30-EP with the efficiency of other photocatalysts: F-g-C₃N₄-30-EP (5 cm² is equivalent to 10.0 mg/L; this work), (1) Cu-MoS₂ (1.6 mg/L, 100 mW/cm²; Lin et al.¹³), (2) Bulk g-C₃N₄ (150 mg/L, 150 mW/cm² for MS2 inactivation; Wang et al.³⁵), (3) GO-CdS (100 mg/L, 100 mW/cm²; Li et al.³⁷), (4) S-GO-C₃N₄ (100 mg/L, 193 mW/cm²; Ma et al.³³), and (5) single-layer C₃N₄ (100 mg/L, 100 mW/cm²; Li et al.³²).

The inhibition and poisoning of catalyst were also evaluated by the addition of common substances in environmental water for evaluating the practical application of F-g-C₃N₄-30-EP (Figure S28).⁶³ The activity of F-g-C₃N₄-30-EP is strongly dependent on the *K_a* of acid ion and *K_b* of base ion, i.e., if *K_a* << *K_b* (e.g., NaHCO₃, Na₃PO₄), the suspension is alkali so that fewer H⁺ ions participate in the production of H₂O₂,⁵² which inhibits the reaction. Previous investigation showed that humic acid significantly influenced the disinfection activity of TiO₂, the most widely used catalyst for disinfection.⁶³ In our disinfection system, the addition of humic acid only slightly reduced the activity of F-g-C₃N₄-30-EP. This is attributed to the differences in light-absorption ranges of TiO₂ and g-C₃N₄-30. Photon absorption of g-C₃N₄-30 is only slightly influenced because humic acid can strongly absorb UV light rather than visible light.⁶⁴

Furthermore, we also evaluated the solid-poisoning effect (and/or the light-shading effect) by measuring disinfection activity in *E. coli* suspensions with different concentrations (Figure S29). The activities of F-g-C₃N₄-30-EP were reduced when the concentration of bacterial suspension increased because the higher concentration of cell debris and oxidation products appearing in the later

Table 1. Comparison of Photocatalytic Disinfection Experimental Conditions and Disinfection Performance of Recently Reported Heavy-Metal-free Photocatalysts

Sample	Size and Concentration	Light Wavelength and Irradiation Intensity	Bacteria Strain	Disinfection Time and $-\log_{10}(C/C_0)$ Efficiency	Reference
F-g-C ₃ N ₄ -30-EP	5 cm ² film, 10 mg/L	>400 nm, 100 mW/cm ²	<i>E. coli</i> , K-12, <i>Salmonella</i> ATCC 13076	6 in 30 min	this work
Porous g-C ₃ N ₄ nanosheets	400 mg/L	>420 nm	<i>E. coli</i>	2 in 240 min	Martha et al. ²⁹
Bulk g-C ₃ N ₄	150 mg/L	>400 nm, 150 mW/cm ²	MS2	8 in 360 min	Wang et al. ³⁵
g-C ₃ N ₄ /TiO ₂ /kaolinite	30 mg/L	>400 nm	<i>S. aureus</i>	3 in 300 min	Kofuji et al. ³⁰
g-C ₃ N ₄ /TiO ₂	600 mg/L	>420 nm, 30 mW/cm ²	<i>E. coli</i> , K-12	7 in 180 min	Zhao et al. ³⁴
S-GO-C ₃ N ₄	100 mg/L	>400 nm, 193 mW/cm ²	<i>E. coli</i> , K-12	5 in 240 min	Ma et al. ³³
SL-C ₃ N ₄	100 mg/L	>400 nm, 100 mW/cm ²	<i>E. coli</i> , K-12	7 in 240 min	Li et al. ³²
Cu-MoS ₂ ^a	2 cm ² film, 1.6 mg/L	>400 nm, 100 mW/cm ²	<i>E. coli</i> , K-12, <i>E. coli</i> JM109	5 in 20 min	Liu et al. ¹³
Ag-C ₃ N ₄	20 mg/L	>400 nm	<i>E. coli</i>	7 in 90 min	Xu et al. ³¹
CoFe ₂ O ₄ /HTCC	1000 mg/L	>400 nm	<i>E. coli</i> , K-12	7 in 60 min	Li et al. ³⁸
Bi ₂ MoO ₆ /C ₃ N ₄	100 mg/L	>420 nm,	<i>E. coli</i>	6 in 300 min	Li et al. ³⁶
Fe ₃ O ₄ @BiOI@Agl	500 mg/L	>400 nm, 100 mW/cm ²	<i>E. coli</i> ATCC15597	8 in 60 min	Gao et al. ³⁹
TiO ₂ -CdS	1 cm ² film	Xenon, 150 mW/cm ²	<i>E. coli</i> , XL1 Blue	2 in 20 min	Hayden et al. ¹⁵
ZnO-Cu	100 mg/L	>400 nm, 100 mW/cm ²	<i>E. coli</i> , ATCC 8739	6 in 30 min	Bai et al. ¹⁶
GO-CdS	100 mg/L	>420 nm, 100 mW/cm ²	<i>E. coli</i> , K-12	6 in 60 min	Li et al. ³⁷
BV	100 mg/L	>400 nm, 193 mW/cm ²	<i>E. coli</i> , K-12	4 in 300 min	Wang et al. ¹⁴
SGO-ZnO-Ag	100 mg/L	>420 nm, 100 mW/cm ²	<i>E. coli</i> , K-12	6 in 30 min	Wang et al. ⁴⁰

E. coli, *Escherichia coli*; *S. aureus*, *Staphylococcus aureus*.

^aCu concentration in solution phrase was 3.25 parts per billion ($\mu\text{g L}^{-1}$).

disinfection period usually compete with the radical species, which eliminates the microorganism.^{62,63}

F-g-C₃N₄-30-EP exhibited the best comprehensive catalytic bacterial disinfection performance, which we assessed by comparing its activity and catalyst consumption with those of reported metal-free catalysts, and its performance was comparable to that of the best metal-based catalysts (Figures 4D and S30; Table 1). The first-order disinfection rate of F-g-C₃N₄-30-EP was five times higher than that of the previously reported most efficient metal-free photocatalysts ($k_{SL-C_3N_4} = 0.028 \text{ min}^{-1}$) with only 10% catalyst consumption under light intensity of 100 mW/cm².³⁴ Moreover, the disinfection performances of F-g-C₃N₄-30 and F-g-C₃N₄-30-EP were also compared with those of the standard photocatalyst (P25) under the same experimental conditions (Figure S31). g-C₃N₄-30-based catalyst showed significant improvement in terms of activity even in comparison with the P25 under solar light. Importantly, the fixed metal-free catalyst can eliminate the Trojan-horse effect¹⁰ and heavy-metal threat caused by nanosized photocatalysts. After 30 min of visible-light irradiation, its bacteria residue (<0.0001%) was much lower than that of TiO₂-CdS¹⁵ ($\approx 1\%$) and MoS₂-Cu¹³ (<0.001%), which to our knowledge is the best reported fixed photo-disinfection catalyst.

To further develop the applications of the edge-functionalized C₃N₄ for highly efficient photocatalytic water disinfection, we fixed it onto plastic membrane bags (polyethylene). The as-prepared sol was simply drop-casted onto the internal surface of the silane-modified plastic bags (Figure 5A). These water disinfection bags are

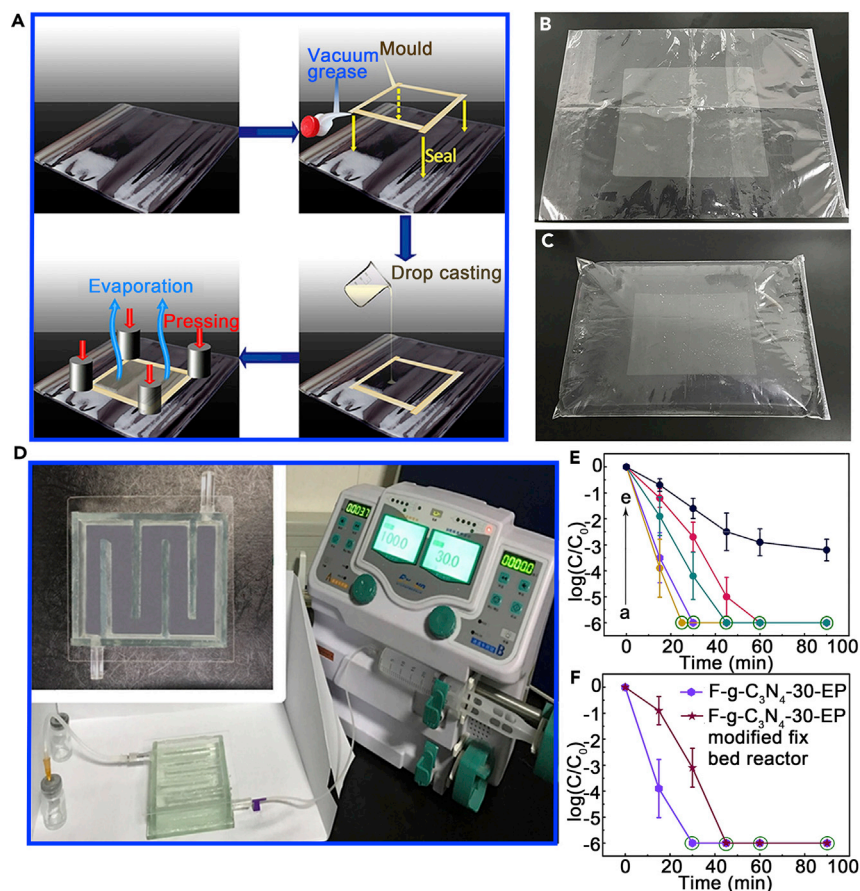


Figure 5. Disinfection Devices Based on F-g-C₃N₄-30-EP

(A) Diagrammatic sketch of the modification process utilizing F-g-C₃N₄-30-EP coated onto a polyethylene bag modified by a silane coupling agent. (B) Photograph of newly prepared F-g-C₃N₄-30-EP-modified polyethylene bags. (C) Photograph of newly prepared F-g-C₃N₄-30-EP-modified polyethylene bag filled with water. (D) Flowing water disinfection device modified by nano-coating of F-g-C₃N₄-30-EP. (E) Comparison of disinfection performance between F-g-C₃N₄-30-EP- and F-g-C₃N₄-30-EP-modified PE bags (under visible-light irradiation) measured in different water depths (a, 2 cm; b, F-g-C₃N₄-30-EP of 5 cm² for 25 mL water disinfection [see Figure 4C]; c, 4 cm; d, 5 cm; e, 10 cm.). (F) Comparison of disinfection performance between F-g-C₃N₄-30-EP- and F-g-C₃N₄-30-EP-modified fixed-bed reactors (under visible-light irradiation). In the disinfection performance curves, error bars represent the standard deviation of five replicate measurements, and the points with dark-green circles indicate that no live bacterium was detected.

portable and can be used in extreme conditions for drinkable water production. Contaminated water was simply poured into the bags (Figures 5B and 5C), and pathogens were killed after these bags were exposed to sunlight by the quickly generated ROS. With a 5.0-cm depth of water, it only takes 1 h for water purification with a $-\log_{10}(C/C_0) = 6$ under solar light irradiation, which meets the standard of drinkable water (GB5749-2006, China). After a 40-cycle test of approximately 60 h, the disinfection performance of this bag showed no obvious decrease (Figure S32), indicating the reliability of the device. The volume of purified water was approximately 10 L, which can provide drinking water for at least four adults per day. The disinfection efficiency was significantly decreased if the depth of water increased to 10.0 cm as a result of a high ratio of water volume (and bacterial

number) to photocatalyst active area and the solar light intensity attenuation (Figures 5E and S33).

We also fabricated a fixed-bed reactor by using g-C₃N₄-30 as the photocatalyst to demonstrate its disinfection effect in flowing water (Figure 5D). The disinfection efficiency was $k = 0.082 \text{ min}^{-1}$ ($R^2 = 0.92$) with a $-\log_{10}(C/C_0) = 6$ in 45 min under solar light irradiation (Figure 5F), which is still much higher than those of other metal-free photocatalysts (Table 1). The reliability and stability of the fixed-bed reactor is also good, as shown in the 40-cycle experiment of approximately 60 h (Figure S34). This fixed-bed reactor can be modified to be a fully automatic water disinfection device, which could provide fundamental guidance for the development of automatic photocatalytic water disinfection systems. Another advantage of these devices is avoiding the evaporation of purified water around $500 \text{ mL}/(\text{m}^2 \cdot \text{h})$ at 286.2 K.

In summary, edge-functionalized graphitic carbon nitride (g-C₃N₄) nanosheets were first utilized for preparing highly efficient metal-free fixed catalyst for solar water disinfection. The as-prepared catalyst film showed an inactivation efficiency of $-\log_{10}(C/C_0) = 6$ (>99.9999%) toward model *E. coli* in 30 min under visible-light irradiation. The first-order disinfection rate ($k_{F-g-C_3N_4-30-EP} = 0.14 \text{ min}^{-1}$; $R^2 = 0.98$) in this work is five times higher than that of the reported best metal-free photocatalysts with a lower catalyst consumption. Importantly, the catalytic activity is comparable with that of the best metal-based photocatalyst in terms of both disinfection efficiency and catalyst consumption. By combining the experimental data and calculated results, we have confirmed that exposed carboxyl (–COOH) and carbonyl (C=O) groups at the edges of g-C₃N₄ nanosheets can significantly induce the upward band bending, facilitate the generation of H₂O₂, and enhance the charge separation, hence improving the catalytic performance. Furthermore, this catalyst can be incorporated into devices, such as polymeric bags and fixed-bed reactors, for clean water production. It is believed that this work could provide a primary guidance for developing photocatalytic water disinfection devices for commercial applications.

EXPERIMENTAL PROCEDURES

Exfoliation of g-C₃N₄ Nanosheets in Different Oxygenous Levels

Bulk-g-C₃N₄ was prepared by thermal condensation using melamine. Oxygen-functionalized g-C₃N₄ nanosheets were prepared by an improved Hummer's method, which has been reported in our previous work.⁴⁸ In brief, the mixture containing bulk-g-C₃N₄, H₂SO₄ and KMnO₄ was heated at 303.2 K with constant stirring, and the heating duration was strictly controlled from 30 to 60 min (30, 45, and 60 min; the as-prepared g-C₃N₄ nanosheets are denoted as g-C₃N₄-30, g-C₃N₄-45, and g-C₃N₄-60, respectively) to yield functionalized g-C₃N₄ nanosheets with different degrees of oxidation. The reduced carbon nitride nanosheets (g-C₃N₄-r) were prepared by reducing g-C₃N₄-60 with hydrazine hydrate.

Preparation of Disinfection Devices by Liquid-Phase Self-Assembly Using the Functionalized g-C₃N₄ Nanosheets

The glass substrate (2.0 cm × 2.5 cm) was treated with piranha solution to achieve surface hydroxylation and to increase the interaction between substrate and modifiers. Suspensions (1.00 mL) of bulk-g-C₃N₄, g-C₃N₄-r, g-C₃N₄-30, g-C₃N₄-45, and g-C₃N₄-60 (0.50 mg/mL) were deposited onto the substrate by a simple drop-casting method. Thereafter, the substrate was dried in a vacuum drying oven with a pressure of 66.7 kPa at 303.15 K for 24 h.

Preparation of Disinfection Devices Using Edge-Exposed g-C₃N₄-30 Assembled Nano-coating

Piranha-solution-treated glass substrate (2.0 cm × 2.5 cm) was also used for drop-casting modification. The edge-exposed g-C₃N₄-30 was dispersed in a water-ethanol mixture (containing 25% ethanol and 1.0 mg/mL octanoic acid). After the g-C₃N₄-30 suspension was cast onto the substrate, the substrate was dried in a vacuum drying oven with a pressure of 66.7 kPa at 303.15 K for 24 h, and then the pressure was adjusted to 5.5 kPa and kept for 48 h to remove the adsorbed octanoic acid. To confirm the complete removal of octanoic acid, the as-prepared substrate was placed in deionized water and was treated with ultrasonic waves. After the centrifugation, the chemical content in liquid supernatant was measured by high-performance liquid chromatography, in which octanoic acid was not found.

Disinfection Performance

Different kinds of bacteria, including *E. coli* (ATCC K-12), *Salmonella* (ATCC 13076), and *Enterococcus faecalis* (ATCC 19433), were cultured to log phase and precipitated by centrifugation at 900 × *g*. Then, the bacteria were washed by phosphate-buffered saline (PBS) twice and dispersed in PBS (10⁹ CFU/mL). The starting concentration of bacteria was adjusted to be 10⁶ CFU/mL, and the bacterial concentration at each time point of the experiment was standardized to the starting concentration. Photocatalytic disinfection was performed with a 300 W xenon lamp (CEL-HXF300H5, CEAULIGHT, Beijing) as the light source, which was calibrated at air mass 1.5 G (100 mW/cm²) and equipped with a UVF (JB400, CEAULIGHT, Beijing) and red-pass filter (MISCUT800, CEAULIGHT, Beijing) to adjust the range of light spectrum. The water volume was 50 mL, and the depth of the aqueous solution was 2.0 cm. Bacterial concentrations were measured by standard spread-plating techniques with different irradiation durations. Each sample was serially diluted, and each dilution was plated in quintuplicate onto solid medium and incubated at 37°C for 16 h. The solar-disinfection experiments were conducted in quintuplicate (*n* = 5). The light spectra (xenon lamp with a UVF or xenon lamp with a red-pass filter) were measured at the same place at which the films of g-C₃N₄ nanosheets were set during the disinfection experiment. The solar spectrum during the real sunlight experiment was estimated by a simple model of the atmospheric radiative transfer of sunshine. The disinfection rates (*k*) were estimated by Chick's law: $\ln(C/C_0) = -kt$, in which *k* is a constant in units of time, *C* is the concentration of bacteria, and *C*₀ is the concentration at *t* = 0. The slope of the best-fitting line for the plot of $\ln(C/C_0)$ versus *t* was used to figure out *k*.

Photo-selective Deposition of Pt Nanoparticles on Carbon Materials

0.5 mL H₂PtCl₆ (1 mg/L) aqueous solution was mixed with 9 mL g-C₃N₄-30 or g-C₃N₄-*r* suspension (1 mg/L) in a 15-mL tube. After N₂ bubbling for 1 h, 0.5 mL 2-propanol was added into the suspension as hole sacrificial reagent. Thereafter, weak UV irradiation (approximately 0.2 mW/cm²) was continued on the tube for 24 h. Afterward, the product was washed with water at least three times to remove the free nanoparticles for further investigation.

SUPPLEMENTAL INFORMATION

Supplemental Information includes detailed descriptions of the apparatus and methods, 34 figures, and 1 table and can be found with this article online at <https://doi.org/10.1016/j.chempr.2018.12.009>.

ACKNOWLEDGMENTS

All authors acknowledge the financial support of the National Natural Science Foundation of China (grants 21375116, 21590795, and 21820102002), the Priority Academic

Program Development of Jiangsu Higher Education Institutions, and the Jiangsu Province Research Program on analytical methods and techniques on the shared platform of large-scale instruments and equipment (BZ 201409). Detailed photo-deposition conditions and disinfection mechanisms were discussed with Professor Teruhisa Ohno of Kyushu Institute of Technology, Japan. DFT calculation was performed by the servers provided by Jian Wang and Yuheng Xing in the College of Physics of Yangzhou University. All authors acknowledge their significant contribution.

AUTHOR CONTRIBUTIONS

G.W. and C.W. conceived the project. Z.T., N.Y., C.W., D.W., and G.W. designed, analyzed, and discussed the experimental results and drafted the manuscript. Z.T. synthesized the compounds and collected most spectral data. Z.T. and S.W. performed DFT calculations. M.H. and Z.T. performed the disinfection experiment. Z.T. and H.L. performed the photoelectric test and analysis. H.L. performed the X-ray analysis. Z.T. and S.W. designed and prepared disinfection devices.

DECLARATION OF INTERESTS

The authors declare no competing interests.

Received: July 29, 2018

Revised: August 30, 2018

Accepted: December 11, 2018

Published: February 7, 2019

REFERENCES AND NOTES

- Shannon, M.A., Bohn, P.W., Elimelech, M., Georgiadis, J.G., Mariñas, B.J., and Mayes, A.M. (2008). Science and technology for water purification in the coming decades. *Nature* 452, 301–310.
- Logan, B.E., and Elimelech, M. (2012). Membrane-based processes for sustainable power generation using water. *Nature* 488, 313–319.
- Prasad, K.P., Than, A., Li, N., Alam SK, M., Duan, H., Pu, K., Zheng, X., and Chen, P. (2017). Thiophene-derived polymer dots for imaging endocytic compartments in live cells and broad-spectrum bacterial killing. *Mater. Chem. Front.* 1, 152–157.
- Hsu, C.-L., Lien, C., Harroun, S.G., Ravindranath, R., Chang, H., Mao, J., and Huang, C. (2017). Metal-deposited bismuth oxyiodide nanonetworks with tunable enzyme-like activity: sensing of mercury and lead ions. *Mater. Chem. Front.* 1, 893–899.
- Liu, C., Xie, X., Zhao, W., Yao, J., Kong, D., Boehm, A.B., and Cui, Y. (2014). Static electricity powered copper oxide nanowire microbicidal electroporation for water disinfection. *Nano Lett.* 14, 5603–5608.
- Loeb, S., Hofmann, R., and Kim, J.-H. (2016). Beyond the pipeline: Assessing the efficiency limits of advanced technologies for solar water disinfection. *Environ. Sci. Technol. Lett.* 3, 73–80.
- Chong, M.N., Jin, B., Chow, C.W.K., and Saint, C. (2010). Recent developments in photocatalytic water treatment technology: A review. *Water Res.* 44, 2997–3027.
- Mao, C., Xiang, Y., Liu, X., Cui, Z., Yang, X., Yeung, K.W.K., Pan, H., Wang, X., Chu, P.K., and Wu, S. (2017). Photo-inspired antibacterial activity and wound healing acceleration by hydrogel embedded with Ag/Ag@AgCl/ZnO nanostructures. *ACS Nano* 11, 9010–9021.
- Chen, X., and Mao, S.S. (2007). Titanium dioxide nanomaterials: Synthesis, properties, modifications, and applications. *Chem. Rev.* 107, 2891–2959.
- Valsami-Jones, E., and Lynch, I. (2015). How safe are nanomaterials? *Science* 350, 388–389.
- Wang, Z., and Mi, B. (2017). Environmental applications of 2D molybdenum disulfide (MoS₂) nanosheets. *Environ. Sci. Technol.* 51, 8229–8244.
- Zeng, X., Wang, Z., Wang, G., Gengenbach, T.R., McCarthy, D.T., Deletic, A., Yu, J., and Zhang, X. (2017). Highly dispersed TiO₂ nanocrystals and WO₃ nanorods on reduced graphene oxide: Z-scheme photocatalysis system for accelerated photocatalytic water disinfection. *Appl. Catal. B* 218, 163–173.
- Liu, C., Kong, D., Hsu, P.-C., Yuan, H., Lee, H.-W., Liu, Y., Wang, H., Wang, S., Yan, K., Lin, D., et al. (2016). Rapid water disinfection using vertically aligned MoS₂ nanofilms and visible light. *Nat. Nano* 11, 1098–1104.
- Wang, W., Yu, Y., An, T., Li, G., Yip, H.Y., Yu, J.C., and Wong, P.K. (2012). Visible-light-driven photocatalytic inactivation of *E. coli* K-12 by bismuth vanadate nanotubes: Bactericidal performance and mechanism. *Environ. Sci. Technol.* 46, 4599–4606.
- Hayden, S.C., Allam, N.K., and El-Sayed, M.A. (2010). TiO₂ nanotube/CdS hybrid electrodes: Extraordinary enhancement in the inactivation of *Escherichia coli*. *J. Am. Chem. Soc.* 132, 14406–14408.
- Bai, H., Liu, Z., and Sun, D.D. (2011). Hierarchical ZnO/Cu "corn-like" materials with high photodegradation and antibacterial capability under visible light. *Phys. Chem. Chem. Phys.* 13, 6205–6210.
- Whitby, R.L.D. (2014). Chemical control of graphene architecture: Tailoring shape and properties. *ACS Nano* 8, 9733–9754.
- Liao, L., Peng, H., and Liu, Z. (2014). Chemistry makes graphene beyond graphene. *J. Am. Chem. Soc.* 136, 12194–12200.
- Avouris, P. (2010). Graphene: Electronic and photonic properties and devices. *Nano Lett.* 10, 4285–4294.
- Georgakilas, V., Permana, J.A., Tucek, J., and Zboril, R. (2015). Broad family of carbon nanoallotropes: Classification, chemistry, and applications of fullerenes, carbon dots, nanotubes, graphene, nanodiamonds, and combined superstructures. *Chem. Rev.* 115, 4744–4822.
- Wang, X., Maeda, K., Thomas, A., Takahashi, K., Xin, G., Carlsson, J.M., Domen, K., and Antonietti, M. (2009). A metal-free polymeric photocatalyst for hydrogen production from water under visible light. *Nat. Mater.* 8, 76–80.
- Huang, J., Ho, W., and Wang, X. (2014). Metal-free disinfection effects induced by graphitic

- carbon nitride polymers under visible light illumination. *Chem. Commun.* **50**, 4338–4340.
23. Wang, Y., Wang, X., and Antonietti, M. (2012). Polymeric graphitic carbon nitride as a heterogeneous organocatalyst: From photochemistry to multipurpose catalysis to sustainable chemistry. *Angew. Chem. Int. Ed.* **51**, 68–89.
 24. Ong, W.-J., Tan, L.-L., Ng, Y.H., Yong, S.-T., and Chai, S.-P. (2016). Graphitic carbon nitride (g-C₃N₄)-Based photocatalysts for artificial photosynthesis and environmental remediation: Are we a step closer to achieving sustainability? *Chem. Rev.* **116**, 7159–7329.
 25. Zhang, J., Chen, Y., and Wang, X. (2015). Two-dimensional covalent carbon nitride nanosheets: Synthesis, functionalization, and applications. *Energy Environ. Sci.* **8**, 3092–3108.
 26. Li, H., Zhao, F., Zhang, J., Luo, L., Xiao, X., Huang, Y., Ji, H., and Tong, Y. (2017). A g-C₃N₄/WO₃ photoanode with exceptional ability for photoelectrochemical water splitting. *Mater. Chem. Front.* **1**, 338–342.
 27. Moon, G.-h., Fujitsuka, M., Kim, S., Majima, T., Wang, X., and Choi, W. (2017). Eco-friendly photochemical production of H₂O₂ through O₂ reduction over carbon nitride frameworks incorporated with multiple heteroelements. *ACS Catal.* **7**, 2886–2895.
 28. Kofuji, Y., Ohkita, S., Shiraishi, Y., Sakamoto, H., Tanaka, S., Ichikawa, S., and Hirai, T. (2016). Graphitic carbon nitride doped with biphenyl diimide: Efficient photocatalyst for hydrogen peroxide production from water and molecular oxygen by sunlight. *ACS Catal.* **6**, 7021–7029.
 29. Martha, S., Mansingh, S., Parida, K.M., and Thirumurugan, A. (2017). Exfoliated metal free homojunction photocatalyst prepared by a biomediated route for enhanced hydrogen evolution and rhodamine b degradation. *Mater. Chem. Front.* **1**, 1641–1653.
 30. Kofuji, Y., Isobe, Y., Shiraishi, Y., Sakamoto, H., Tanaka, S., Ichikawa, S., and Hirai, T. (2016). Carbon nitride-aromatic diamide-graphene nanohybrids: Metal-free photocatalysts for solar-to-hydrogen peroxide energy conversion with 0.2% efficiency. *J. Am. Chem. Soc.* **138**, 10019–10025.
 31. Xu, J., Wang, Z., and Zhu, Y. (2017). Enhanced visible-light-driven photocatalytic disinfection performance and organic pollutant degradation activity of porous g-C₃N₄ nanosheets. *ACS Appl. Mater. Interfaces* **9**, 27727–27735.
 32. Li, C., Sun, Z., Zhang, W., Yu, C., and Zheng, S. (2018). Highly efficient g-C₃N₄/TiO₂/kaolinite composite with novel three-dimensional structure and enhanced visible light responding ability towards ciprofloxacin and *S. aureus*. *Appl. Catal. B* **220**, 272–282.
 33. Ma, S., Zhan, S., Jia, Y., Shi, Q., and Zhou, Q. (2016). Enhanced disinfection application of Ag-modified g-C₃N₄ composite under visible light. *Appl. Catal. B* **186**, 77–87.
 34. Zhao, H., Yu, H., Quan, X., Chen, S., Zhang, Y., Zhao, H., and Wang, H. (2014). Fabrication of atomic single layer graphitic-C₃N₄ and its high performance of photocatalytic disinfection under visible light irradiation. *Appl. Catal. B* **152–153**, 46–50.
 35. Wang, W., Yu, J.C., Xia, D., Wong, P.K., and Li, Y. (2013). Graphene and g-C₃N₄ nanosheets cocrapped elemental α-sulfur as a novel metal-free heterojunction photocatalyst for bacterial inactivation under visible-light. *Environ. Sci. Technol.* **47**, 8724–8732.
 36. Li, G., Nie, X., Chen, J., Jiang, Q., An, T., Wong, P.K., Zhang, H., Zhao, H., and Yamashita, H. (2015). Enhanced visible-light-driven photocatalytic inactivation of *Escherichia coli* using g-C₃N₄/TiO₂ hybrid photocatalyst synthesized using a hydrothermal-calcination approach. *Water Res.* **86**, 17–24.
 37. Li, Y., Zhang, C., Shuai, D., Naraginti, S., Wang, D., and Zhang, W. (2016). Visible-light-driven photocatalytic inactivation of MS2 by metal-free g-C₃N₄: Virucidal performance and mechanism. *Water Res.* **106**, 249–258.
 38. Li, J., Yin, Y., Liu, E., Ma, Y., Wan, J., Fan, J., and Hu, X. (2017). In situ growing Bi₂MoO₆ on g-C₃N₄ nanosheets with enhanced photocatalytic hydrogen evolution and disinfection of bacteria under visible light irradiation. *J. Hazard. Mater.* **321**, 183–192.
 39. Gao, P., Liu, J., Sun, D.D., and Ng, W. (2013). Graphene oxide-CdS composite with high photocatalytic degradation and disinfection activities under visible light irradiation. *J. Hazard. Mater.* **250–251**, 412–420.
 40. Wang, T., Jiang, Z., An, T., Li, G., Zhao, H., and Wong, P.K. (2018). Enhanced visible-light-driven photocatalytic bacterial inactivation by ultrathin carbon-coated magnetic cobalt ferrite nanoparticles. *Environ. Sci. Technol.* **52**, 4774–4784.
 41. Liang, J., Liu, F., Li, M., Liu, W., and Tong, M. (2018). Facile synthesis of magnetic Fe₃O₄@BiOI@AgI for water decontamination with visible light irradiation: Different mechanisms for different organic pollutants degradation and bacterial disinfection. *Water Res.* **137**, 120–129.
 42. Gao, P., Ng, K., and Sun, D.D. (2013). Sulfonated graphene oxide-ZnO-Ag photocatalyst for fast photodegradation and disinfection under visible light. *J. Hazard. Mater.* **262**, 826–835.
 43. Kan, E., Li, Z., Yang, J., and Hou, J.G. (2008). Half-metallicity in edge-modified zigzag graphene nanoribbons. *J. Am. Chem. Soc.* **130**, 4224–4225.
 44. Rudberg, E., Safek, P., and Luo, Y. (2007). Nonlocal exchange interaction removes half-metallicity in graphene nanoribbons. *Nano Lett.* **7**, 2211–2213.
 45. Son, Y.-W., Cohen, M.L., and Louie, S.G. (2006). Energy gaps in graphene nanoribbons. *Phys. Rev. Lett.* **97**, 216803.
 46. Sharma, R., Nair, N., and Strano, M.S. (2009). Structure-reactivity relationships for graphene nanoribbons. *J. Phys. Chem. C* **113**, 14771–14777.
 47. Wang, X., Li, X., Zhang, L., Yoon, Y., Weber, P.K., Wang, H., Guo, J., and Dai, H. (2009). N-doping of graphene through electrothermal reactions with ammonia. *Science* **324**, 768–771.
 48. Teng, Z., Lv, H., Wang, C., Xue, H., Pang, H., and Wang, G. (2017). Bandgap engineering of ultrathin graphene-like carbon nitride nanosheets with controllable oxygenous functionalization. *Carbon* **113**, 63–75.
 49. Corp, K.L., and Schlenker, C.W. (2017). Ultrafast spectroscopy reveals electron-transfer cascade that improves hydrogen evolution with carbon nitride photocatalysts. *J. Am. Chem. Soc.* **139**, 7904–7912.
 50. Ganguly, P., Byrne, C., Breen, A., and Pillai, S.C. (2018). Antimicrobial activity of photocatalysts: Fundamentals, mechanisms, kinetics and recent advances. *Appl. Catal. B* **225**, 51–75.
 51. Nosaka, Y., Yamashita, Y., and Fukuyama, H. (1997). Application of chemiluminescent probe to monitoring superoxide radicals and hydrogen peroxide in TiO₂ photocatalysis. *J. Phys. Chem. B* **101**, 5822–5827.
 52. Nosaka, Y., and Nosaka, A.Y. (2017). Generation and detection of reactive oxygen species in photocatalysis. *Chem. Rev.* **117**, 11302–11336.
 53. Richard, T. (1996). Calculating the oxygen diffusion coefficient in water (Cornell Waste Management Institute). <http://compost.css.cornell.edu/oxygen/oxygen.diff.water.html>.
 54. Schweitzer, C., and Schmidt, R. (2003). Physical mechanisms of generation and deactivation of singlet oxygen. *Chem. Rev.* **103**, 1685–1758.
 55. Xia, D., Wang, W., Yin, R., Jiang, Z., An, T., Li, G., Zhao, H., and Wong, P.K. (2017). Enhanced photocatalytic inactivation of *Escherichia coli* by a novel Z-scheme g-C₃N₄/m-Bi₂O₄ hybrid photocatalyst under visible light: The role of reactive oxygen species. *Appl. Catal. B* **214**, 23–33.
 56. Zhang, Z., and Yates, J.T. (2012). Band bending in semiconductors: Chemical and physical consequences at surfaces and interfaces. *Chem. Rev.* **112**, 5520–5551.
 57. Ohno, T., Sarukawa, K., and Matsumura, M. (2002). Crystal faces of rutile and anatase TiO₂ particles and their roles in photocatalytic reactions. *New J. Chem.* **26**, 1167–1170.
 58. Osako, K., Matsuzaki, K., Susaki, T., Ueda, S., Yin, G., Yamaguchi, A., Hosono, H., and Miyauchi, M. (2018). Direct observation of interfacial charge transfer between rutile TiO₂ and ultrathin CuO_x film by visible-light illumination and its application for efficient photocatalysis. *ChemCatChem* **10**, 3666–3670.
 59. Zheng, Y., Jiao, Y., Chen, J., Liu, J., Liang, J., Du, A., Zhang, W., Zhu, Z., Smith, S.C., Jaroniec, M., et al. (2011). Nanoporous graphitic-C₃N₄@carbon metal-free electrocatalysts for highly efficient oxygen reduction. *J. Am. Chem. Soc.* **133**, 20116–20119.

60. Lu, X., Yim, W.-L., Suryanto, B.H.R., and Zhao, C. (2015). Electrocatalytic oxygen evolution at surface-oxidized multiwall carbon nanotubes. *J. Am. Chem. Soc.* *137*, 2901–2907.
61. Zhao, Y.-H., Zhu, X.-Y., Wee, K.-H., and Bai, R. (2010). Achieving highly effective non-biofouling performance for polypropylene membranes modified by UV-induced surface graft polymerization of two oppositely charged monomers. *J. Phys. Chem. B* *114*, 2422–2429.
62. Muñoz-Batista, M.J., Fontelles-Carceller, O., Ferrer, M., Fernández-García, M., and Kubacka, A. (2016). Disinfection capability of Ag/g-C₃N₄ composite photocatalysts under UV and visible light illumination. *Appl. Catal. B* *183*, 86–95.
63. Marugán, J., van Grieken, R., Sordo, C., and Cruz, C. (2008). Kinetics of the photocatalytic disinfection of *Escherichia coli* suspensions. *Appl. Catal. B* *82*, 27–36.
64. Uyguner, C.S., and Bekbolet, M. (2005). Evaluation of humic acid photocatalytic degradation by UV-vis and fluorescence spectroscopy. *Cat. Today* *101*, 267–274.

Chem, Volume 5

Supplemental Information

Edge-Functionalized g-C₃N₄ Nanosheets

as a Highly Efficient Metal-free

Photocatalyst for Safe Drinking Water

Zhenyuan Teng, Nailiang Yang, Hongying Lv, Sicong Wang, Maozhi Hu, Chengyin Wang, Dan Wang, and Guoxiu Wang

This PDF file includes:

Apparatus and Methods.

Figure S1 to S34.

Table S1.

S1. Apparatus and Methods**S1.1. Apparatus**

High resolution transmission electron microscopy (HRTEM) images, selected area electron diffraction (SAED) patterns and energy-dispersive X-ray spectroscopy (EDS) mappings were taken on a Tecnai G2 F30 S-Twin electron microscope with an accelerating voltage of 300 kV. X-ray photoelectron spectroscopy (XPS) was performed on an ESCALAB 250Xi (Thermo Scientific, USA). Ultra-violet diffuse reflectance spectra (UV-DRS) was conducted on a UV-Vis-NIR spectrophotometer Cary 5000 (Varian, USA). Electrochemical and photo-electrochemical performances were measured in a three-electrode quartz cell system using a platinum plate as counter electrode, saturated calomel electrode (SCE) as reference electrode, and F-g-C₃N₄ coated ITO glass as the working electrode. The active area of F-g-C₃N₄ samples was 1.5 cm². The electrolyte was 0.1 mol/L Na₂SO₄. The photoelectrochemical experiment results were recorded using an electrochemical station (CHI660B, Shanghai Chenhua Co., China). Visible light irradiation was obtained from a 300 W Xenon lamp (CEL-HXF300H5, CEAULIGHT, Beijing). The photocurrent responses under visible light illumination on or off were measured at 0.0 V. Electrochemical impedance spectra (EIS) were measured at 0.0 V over the frequency range of 0.05-105 Hz with an alternating voltage of 5 mV. The ITO coated with catalyst was also used for Mott-Schottky (MS) measurement but in the dark. The scan rate was 25 mV/s, and the scan frequency was 1 kHz. Electron spin resonance (ESR) signals of spin-trapped paramagnetic species with 5,5-dimethyl-1-pyrroline N-oxide (DMPO) were recorded with a A300-10/12 spectrometer. Under solar light irradiation, different

kinds of photocatalytic disinfectants, including bulk-g-C₃N₄, g-C₃N₄-30, g-C₃N₄-45, g-C₃N₄-60 and g-C₃N₄-r, were tested using DMPO as a radical trapper. All tests were conducted using methanol as the solvent to prevent the disproportionation of water and to provide sacrificial reagent for reactions in holes. Zeta potential measurements of carbon nitride samples were performed on a zeta potential analyzer (Zetasizer Nano ZS90, Malvern Instruments Ltd., the UK) under 298 K to measure the isoelectric point of carbon nitride samples. Typically, bulk-g-C₃N₄ (5 mg) was dispersed in 100 mL of aqueous solution by ultrasonication for 30 min. 50 mg/L of suspension of g-C₃N₄-30 and g-C₃N₄-r were prepared for the measurement. In order to obtain the isoelectric point, the pH of the suspension was then adjusted to several values between 2 and 11 by adding 0.25 mol L⁻¹ HCl or NaOH solution using an pH meter (FE20, Mettler-Toledo, LLC). Three zeta potential readings were tested at each pH value, and the average zeta potential at a certain pH value was plotted against the pH value. The pH value at which the zeta potential was zero was taken as the IEP.

S1.2. Calculation method

M_{elem}, M_{elem} with a carbonyl group (M_{elem}-OH) and M_{elem} with a carboxyl group (M_{elem}-COOH) were selected to represent the elementary units of g-C₃N₄, g-C₃N₄-C=O and g-C₃N₄-COOH for calculation, respectively^{S1}. The frequency and electronic structure calculations were conducted via density functional theory (DFT) in the Gaussian 09 program^{S2}, which was carried out by utilizing UB3LYP/6-31 G(d) level of theory. To simulate the photo-generated holes on the edge of the g-C₃N₄-30, the charges of the molecules were set at +1. After optimization, frequencies of each model were computed, and the Milliken charge distributions together with the free energy were also derived.

S1.3. Determination Procedures of ROSs

The concentrations of ROS, including ¹O₂, ·O₂⁻, ·OH, and H₂O₂ in the inactivation systems, were monitored. ¹O₂ steady state concentration was calculated by testing the decay of furfuryl alcohol (FFA, Macklin Inc., F809657) (98%) using high-performance liquid chromatography

(HPLC) (LCQ Deca XP MAX, Thermo, USA). FFA was separated using an isocratic mobile phase (0.1 %, 20 % phosphoric acid and 80 % acetonitrile, pH = 3.75) at a rate of 1 mL/min and detected using UV absorbance at 218 nm. The rate constant for the generation of $^1\text{O}_2$ and FFA is $1.8 \times 10^8 \text{ M}^{-1} \text{ s}^{-1}$. The steady state concentration of $\cdot\text{O}_2^-$ was calculated by measuring the decay of nitroblue tetrazolium (NBT) (Sinopharm Chemical Reagent Co., Ltd, 98%) using UV-vis spectroscopy. NBT has an absorption peak at 260 nm. The rate constant of the $\cdot\text{O}_2^-$ and NBT reaction was $5.9 \times 10^4 \text{ M}^{-1} \text{ s}^{-1}$. The steady state concentration of $\cdot\text{OH}$ was calculated by measuring the amount of $\cdot\text{OH}$ reacting with benzoic acid (Sinopharm Chemical Reagent Co., Ltd, 99%) using HPLC. Hydroxybenzoic acid was separated using a mobile phase (80% acetonitrile and 20% water) at 1 mL/min and detected using UV absorbance at 255 nm for determination of the p-isomer, and 300 nm for determination of the o- and m-isomers. The concentration factor used to convert total hydroxybenzoic acid from p-isomer was 5.87 and the rate constant for the $\cdot\text{OH}$ and benzoic acid reaction is $6.0 \times 10^9 \text{ M}^{-1} \text{ s}^{-1}$. Concentration was measured using an Amplex Red (Macklin Inc., A832878, 98%) fluorescence probe. The fluorescence of the product was monitored. The excitation wavelength was 550 nm, and emission wavelength was 580 nm

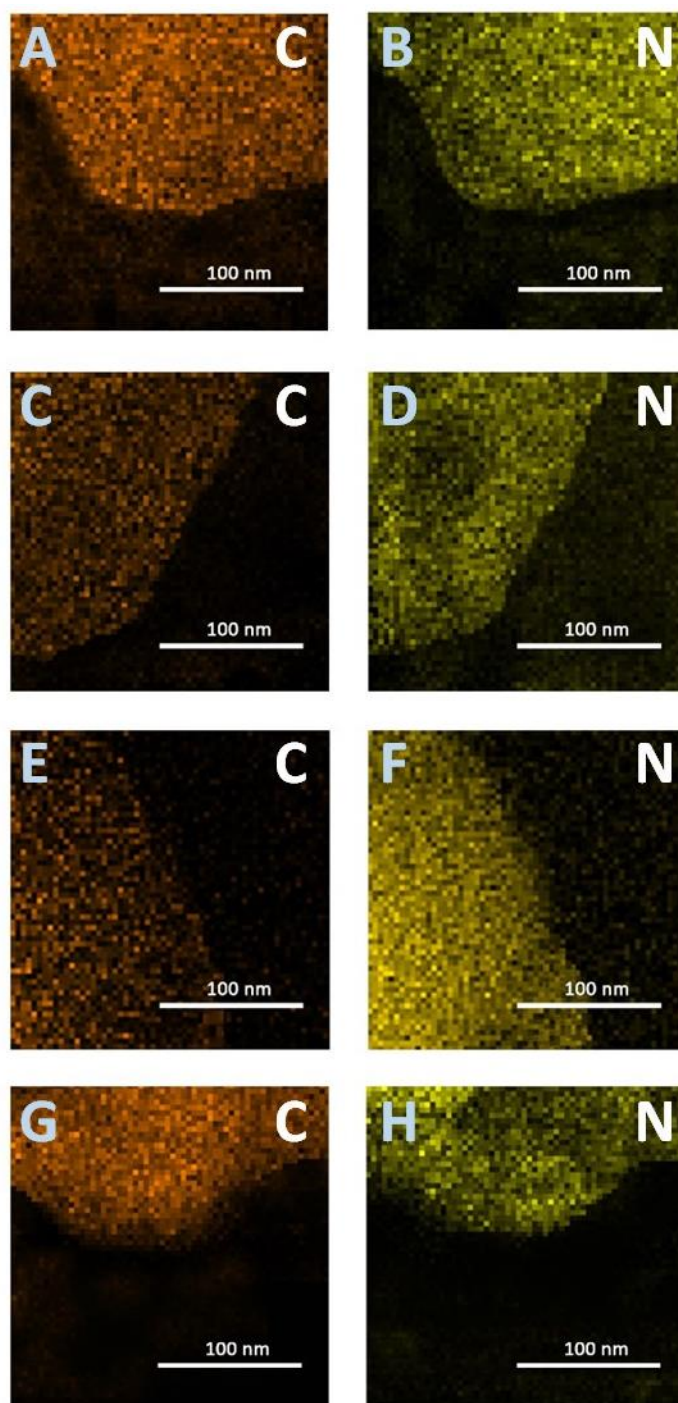


Figure S1. STEM-EDS mappings of g-C₃N₄ nanosheets. (A, C, E, G) carbon and (B, D, F, H) nitrogen distribution in g-C₃N₄-30, g-C₃N₄-45, g-C₃N₄-60 and g-C₃N₄-r, respectively.

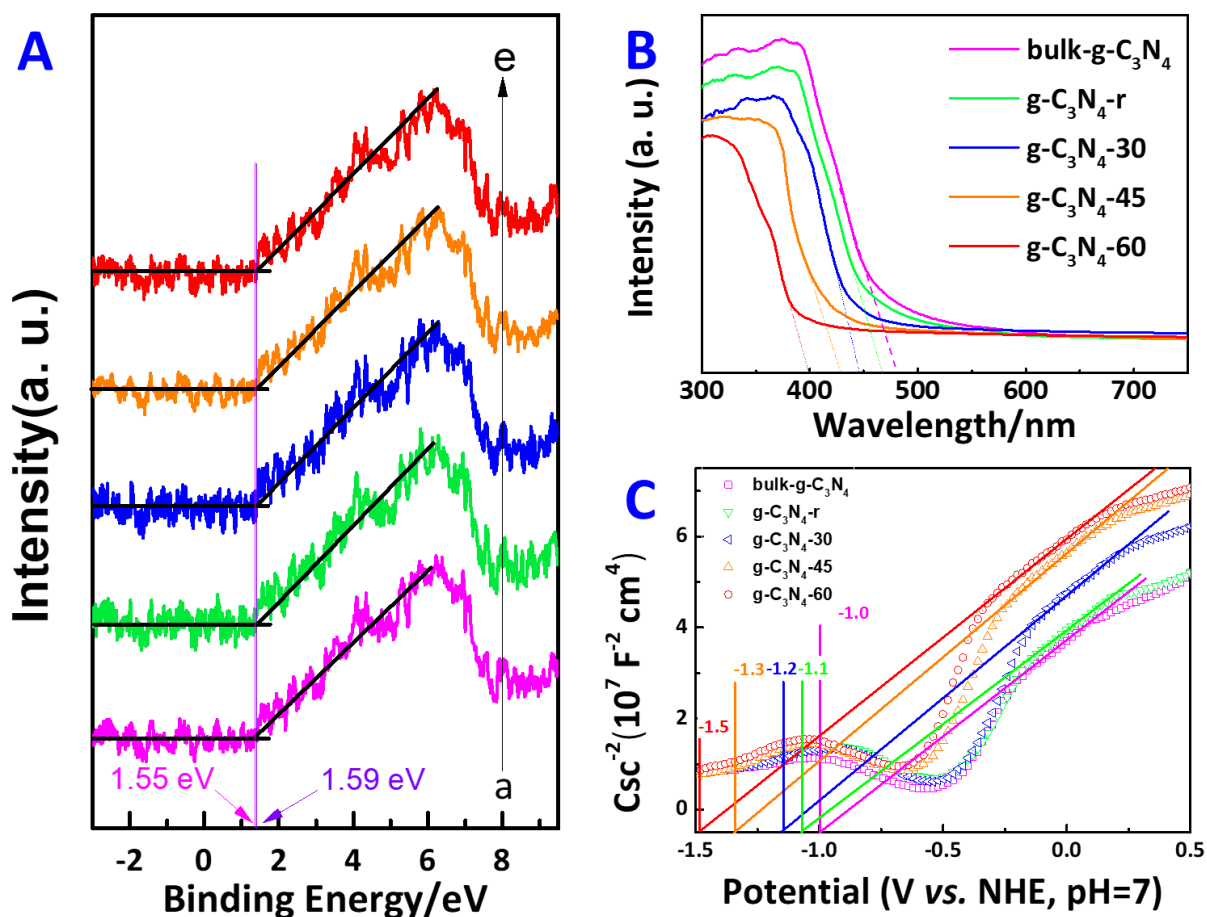


Figure S2. Band positions of g-C₃N₄ samples. (A) Valence band XPS measurements of g-C₃N₄ samples (Line a: bulk-g-C₃N₄; Line b: g-C₃N₄-r; Line c: g-C₃N₄-30; Line d: g-C₃N₄-45; Line e: g-C₃N₄-60); (B) UV-DRS spectra of g-C₃N₄ samples. (C) Mott–Schottky plots of g-C₃N₄ samples (These experiments were performed in the dark. The scan rate was 25 mV/s, and the scan frequency was 1 kHz.).

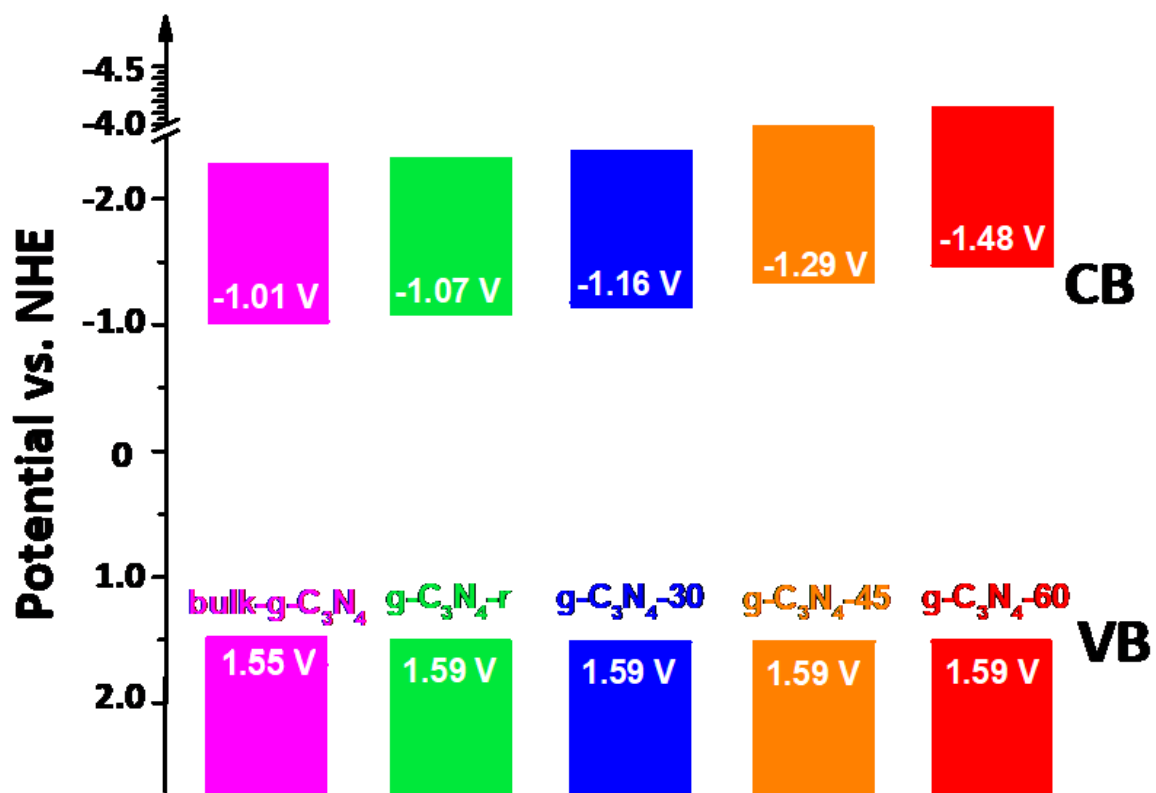


Figure S3. Diagrammatic sketch of the band positions of g-C₃N₄ samples with different oxidation degrees prepared by the improved Hummer's method.

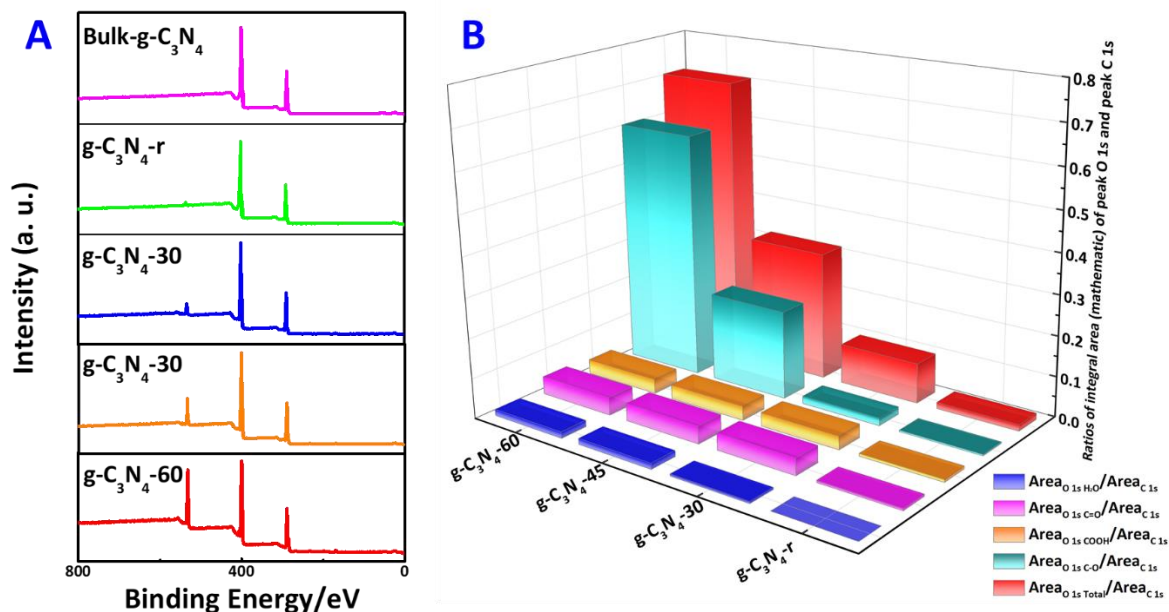


Figure S4. Chemical states distributions of g-C₃N₄ samples. (A) XPS survey spectra for bulk-g-C₃N₄, g-C₃N₄-r, g-C₃N₄-30, g-C₃N₄-45 and g-C₃N₄-60. (B) Ratios of integral area (mathematic) of peak O 1s (H₂O: 523.8 eV; C=O: 531.8 eV; COOH: 530.6 eV; C-O: 533.1 eV; Total oxygen) and peak C 1s in high-resolution O 1s XPS spectra of g-C₃N₄-r, g-C₃N₄-30, g-C₃N₄-45 and g-C₃N₄-60.

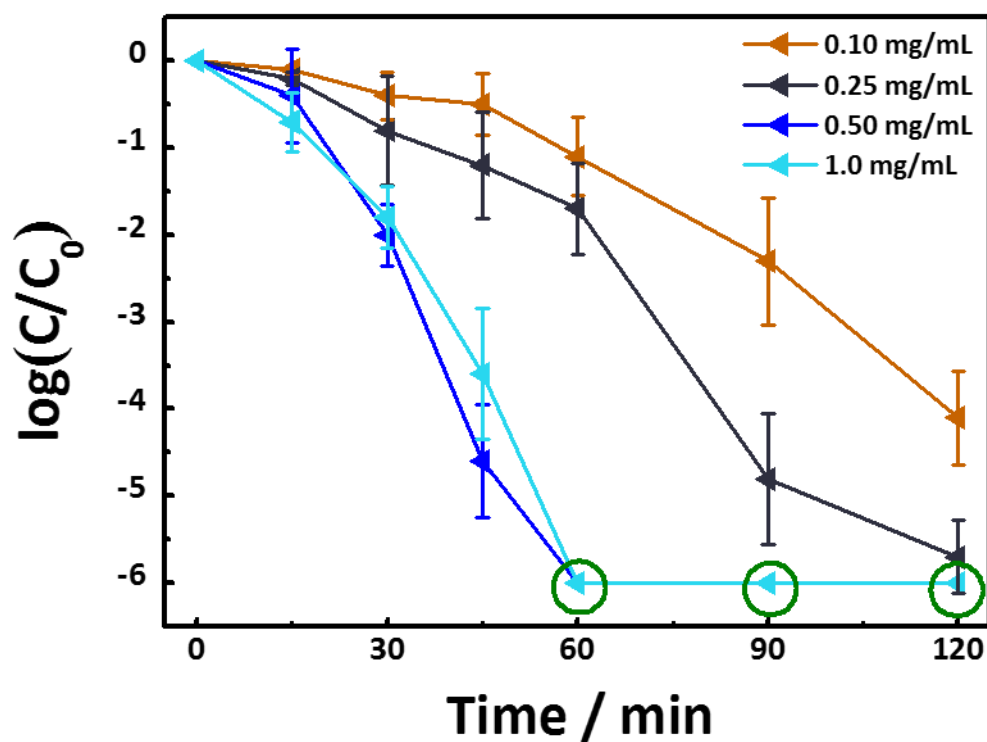


Figure S5. Optimization of modification mass of F-g-C₃N₄-30. The disinfection measurements of g-C₃N₄-30 with different loading mass on 5.0 cm² substrate for 50 mL contaminated water under the illumination of visible light combined with infrared light (Vis+IR, simulated by a xenon lamp with a long-pass filter; $\lambda > 400$ nm). The concentrations of the modifier suspension are shown in the figure. The modification volume of the suspension is 1 mL.

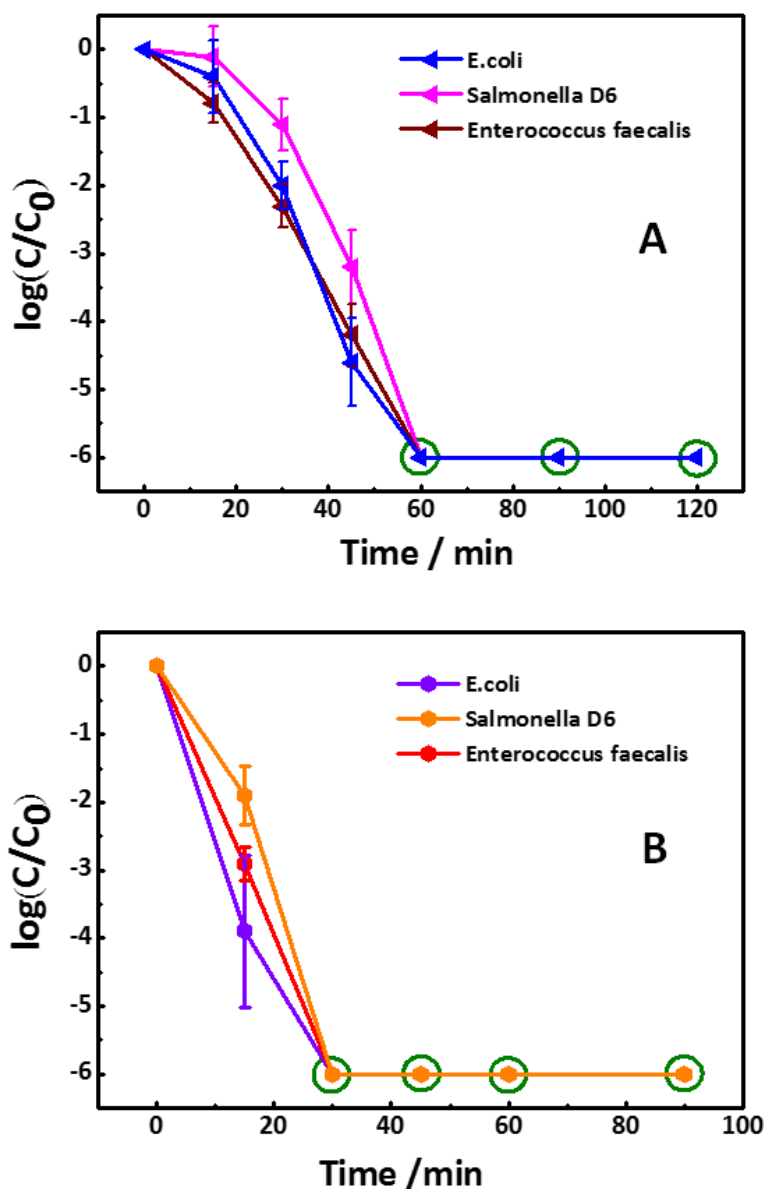


Figure S6. Photocatalytic disinfection of Gram-negative bacteria (*E. coli* and *Salmonella D6*) and Gram-positive bacterium (*Enterococcus faecalis*). (A) Disinfection performance of F-g-C₃N₄-30. (B) Disinfection performance of F-g-C₃N₄-30-EP. In the disinfection performance curves, error bars represent the standard deviation of five replicate measurements and the data point with dark green circle means that no live bacterium was detected. All tests were conducted under visible light combined with infrared light (Vis+IR, simulated by a xenon lamp with a long-pass filter; $\lambda > 400$ nm).

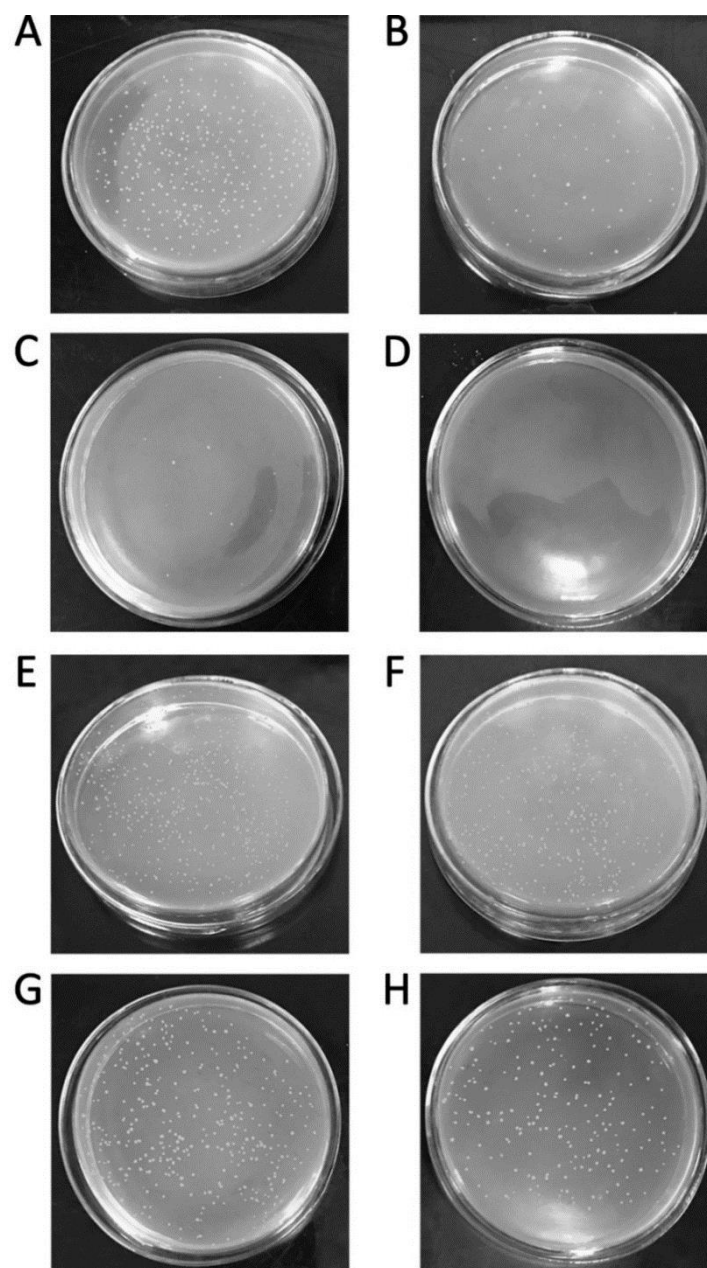


Figure S7. Photos of plate count agars spread with *E. coli* before and after photocatalytic disinfection using F-g-C₃N₄-30: (A) Before, and under solar-light illumination for (B) 15 min; (C) 30 min; (D) 45 min. Photos of plate count agars spread with *E. coli* before and after photocatalytic disinfection without F-g-C₃N₄-30: (E) Before, and under solar-light illumination for (F) 15 min; (G) 30 min; (H) 45 min. The bacteria on plate count agars in all the experiments were incubated at 37.5 °C for 16 h.

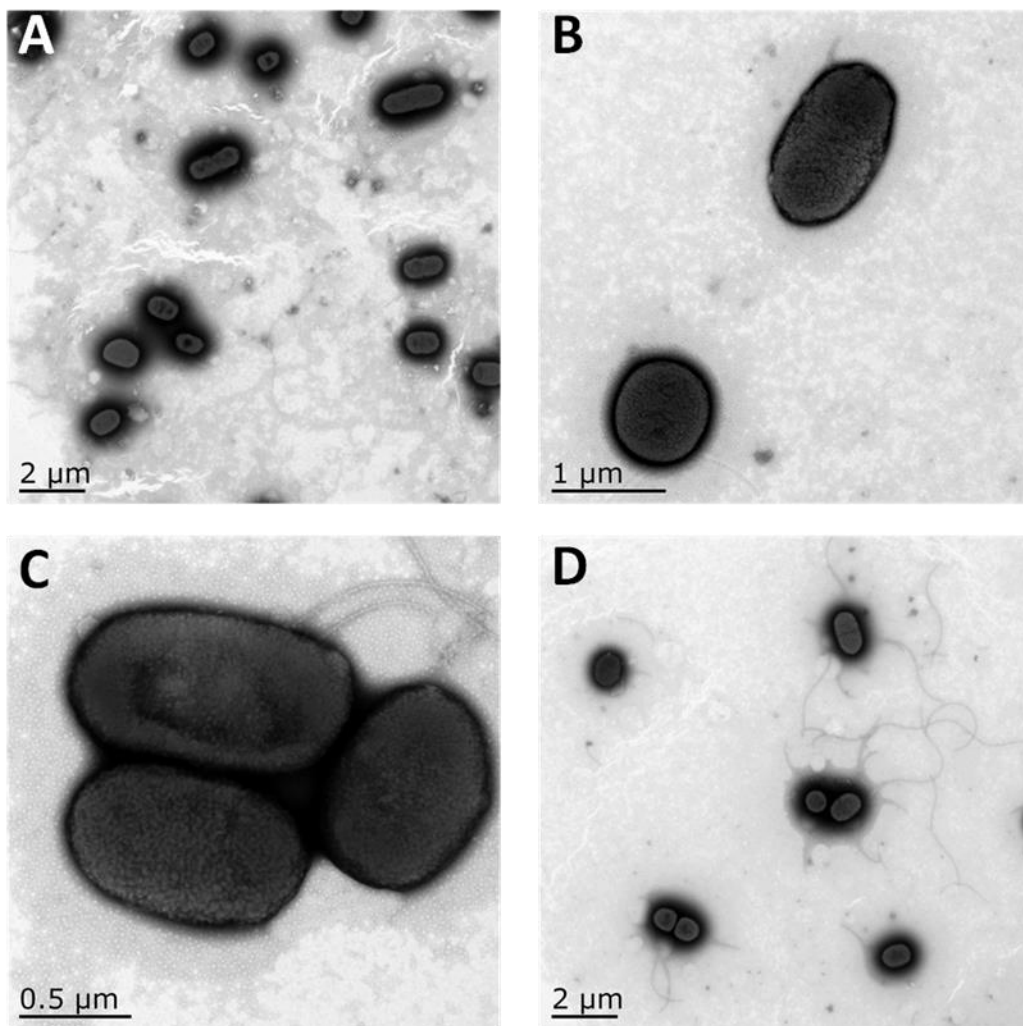


Figure S8. TEM images of *E. coli*. before and after photocatalytic disinfection without F-g-C₃N₄-30: (A) before, and under illumination for (B) 15 min; (C) 30 min; (D) 45 min.

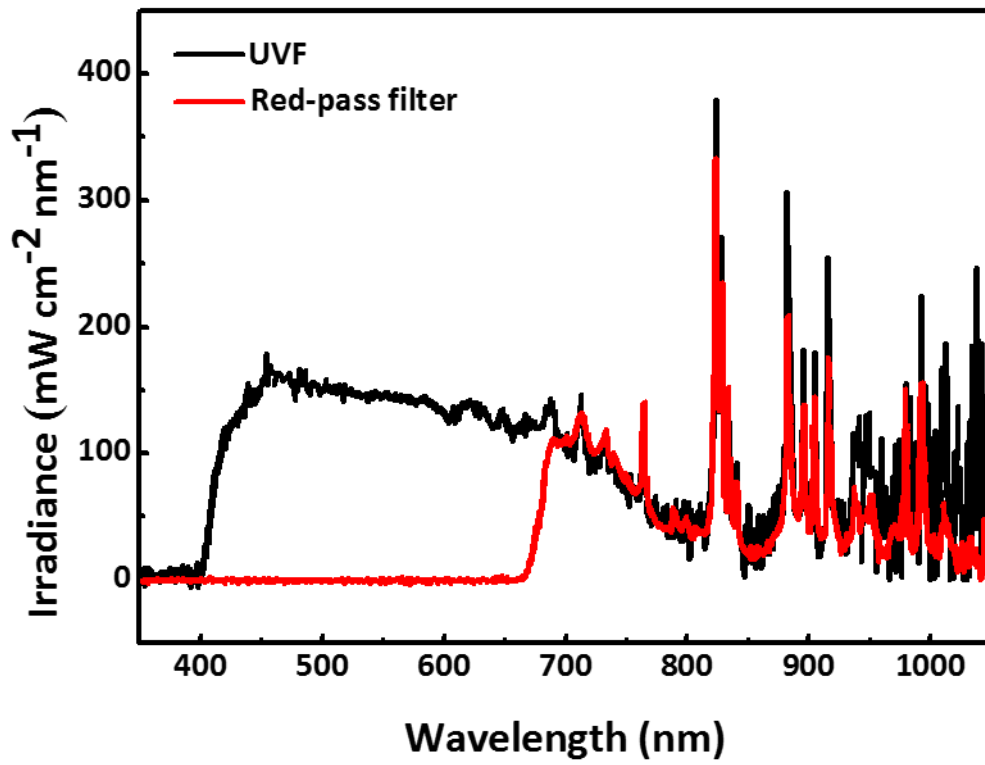


Figure S9. Illumination spectra of different light sources.

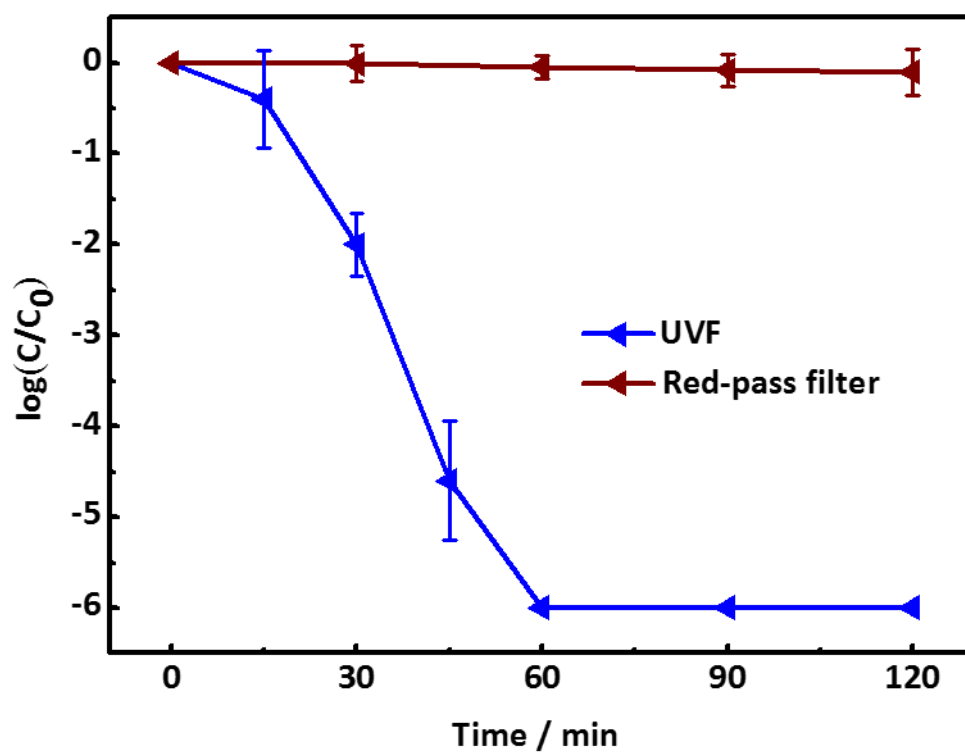


Figure S10. The disinfection performance of F-g-C₃N₄-30 using IR (Brown line) or Vis+IR (Blue line).

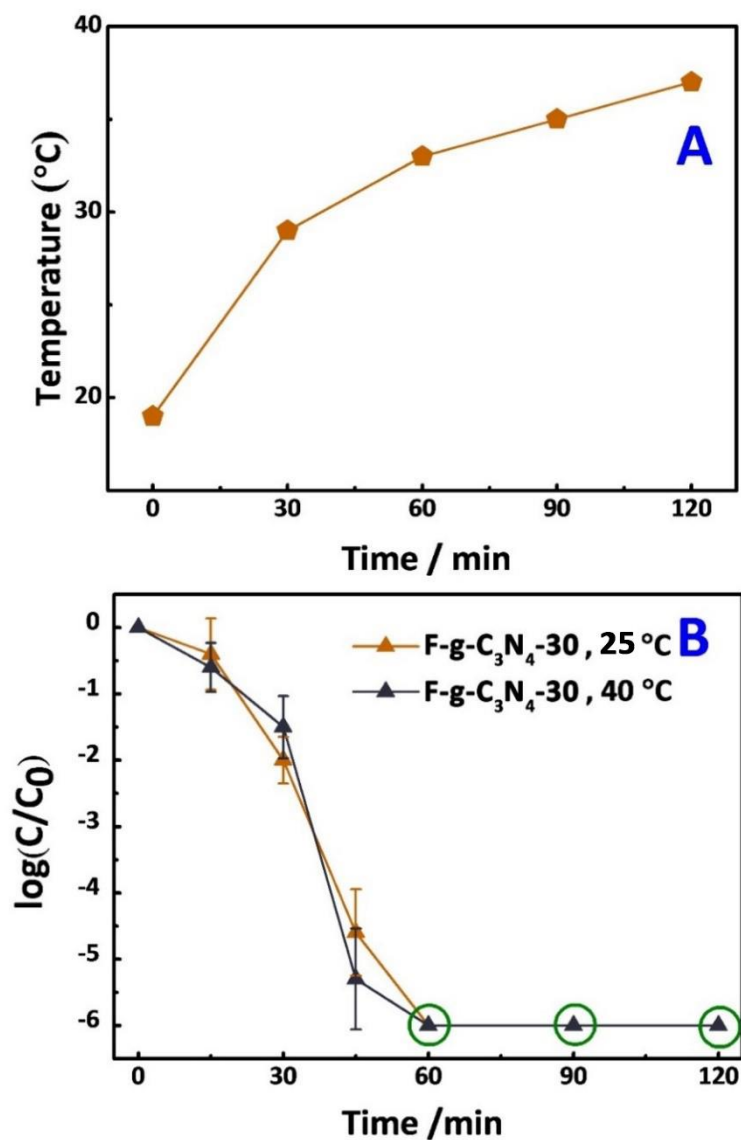


Figure S11. Temperature curve and temperature control experiments for photocatalytic disinfection. (A) Temperature increases with time during photocatalytic disinfection. (B) Comparison between disinfection performance of F-g-C₃N₄-30 at 25 °C (298.2 K,) and at 40 °C (313.2 K) under visible light combined with infrared light (Vis+IR, simulated by a xenon lamp with a long-pass filter; $\lambda > 400$ nm). In the disinfection performance curves, error bars represent the standard deviation of five replicate measurements and the data point with dark green circle indicates that no live bacterium was detected.

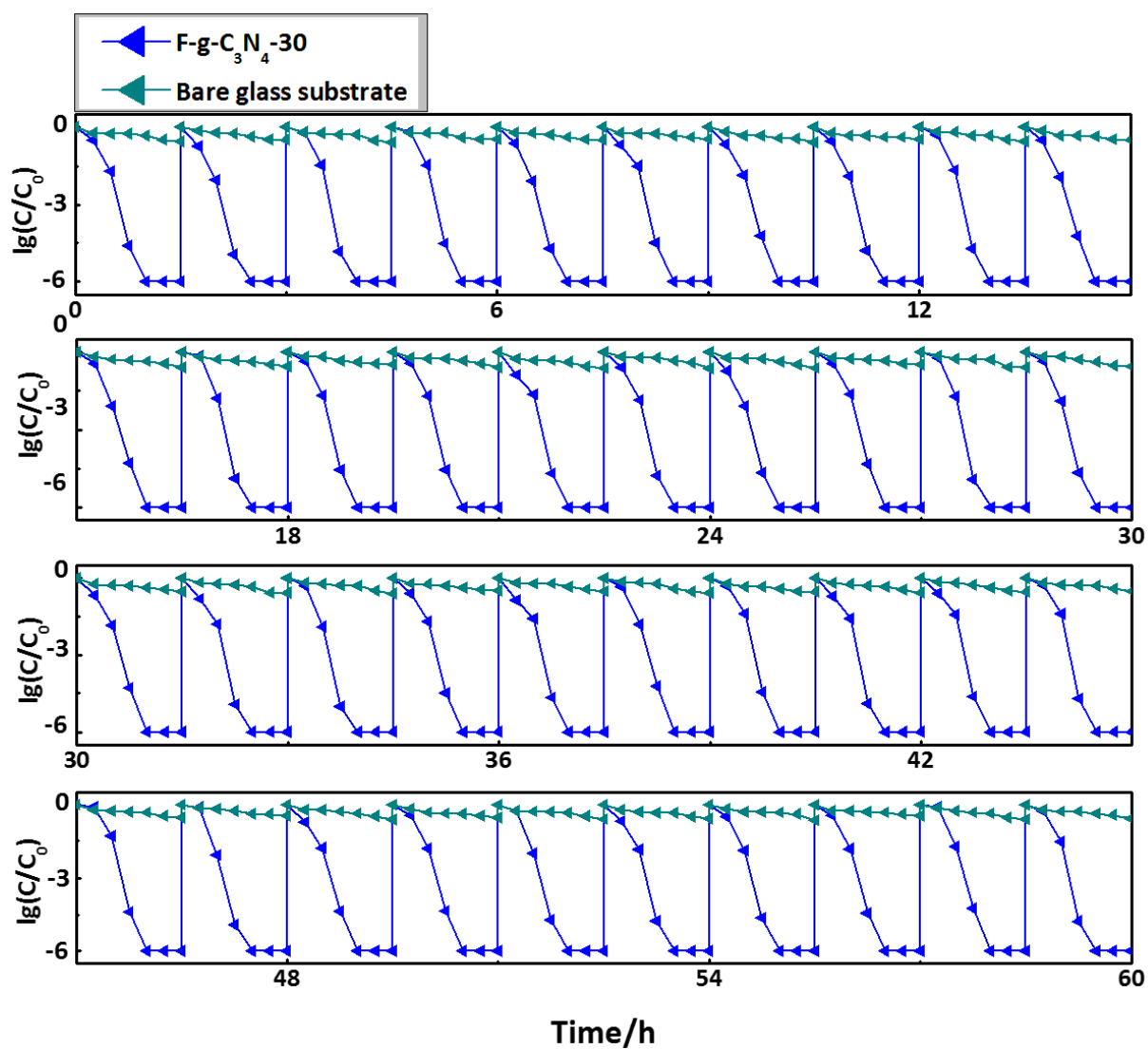


Figure S12. Stability of F-g-C₃N₄-30. Photocatalytic disinfection performance of F-g-C₃N₄-30, which is used for 40 cycles (60 h) under visible light irradiation. After each disinfection circle, the fixed catalyst was washed by deionized water.

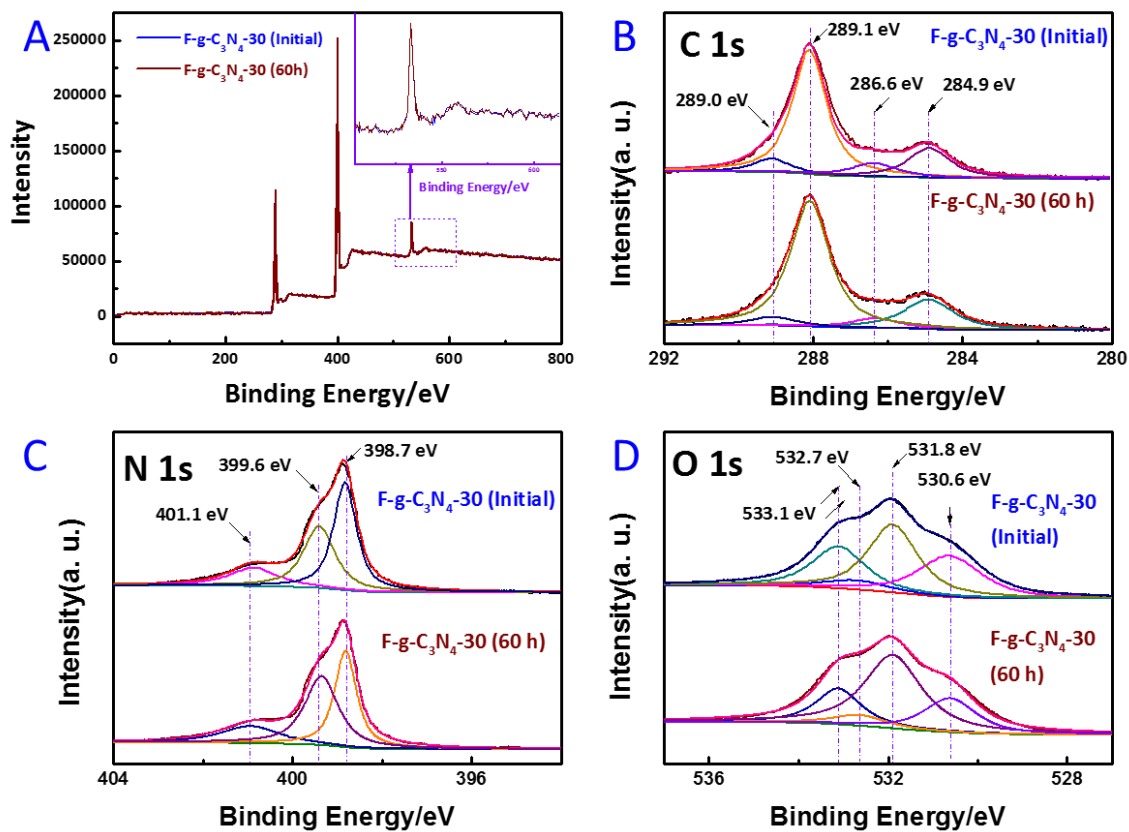


Figure S13. XPS measurements of F-g-C₃N₄-30 and F-g-C₃N₄-30 after continuous disinfection process for 60 h. (A) XPS survey spectra for F-g-C₃N₄-30 and F-g-C₃N₄-30 after continuous photocatalytic disinfection process for 60 h. High-resolution XPS spectra of (B) C 1s, (C) N 1s and (D) O 1s for F-g-C₃N₄-30 and F-g-C₃N₄-30 after continuous photocatalytic disinfection process for 60 h.

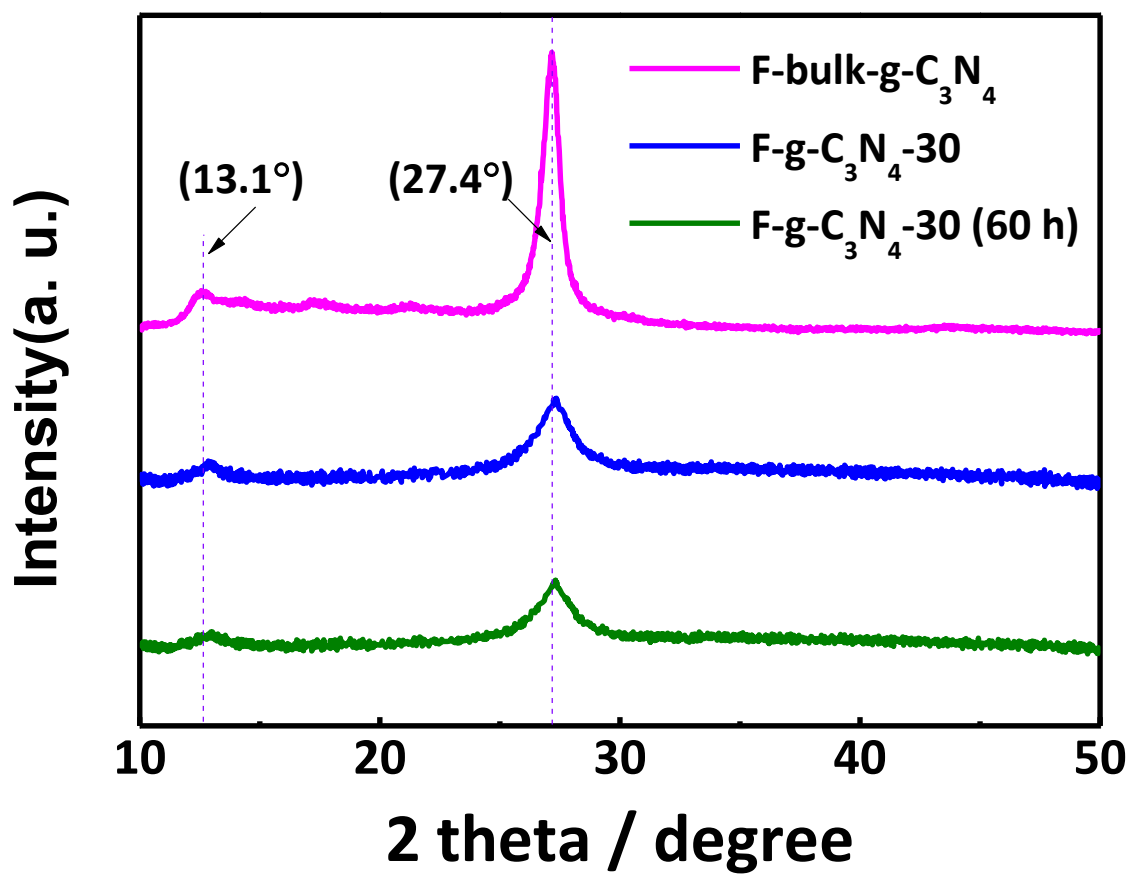


Figure S14. XRD measurements of F-g-C₃N₄-30 and F-g-C₃N₄-30 after continuous disinfection process for 60 h.

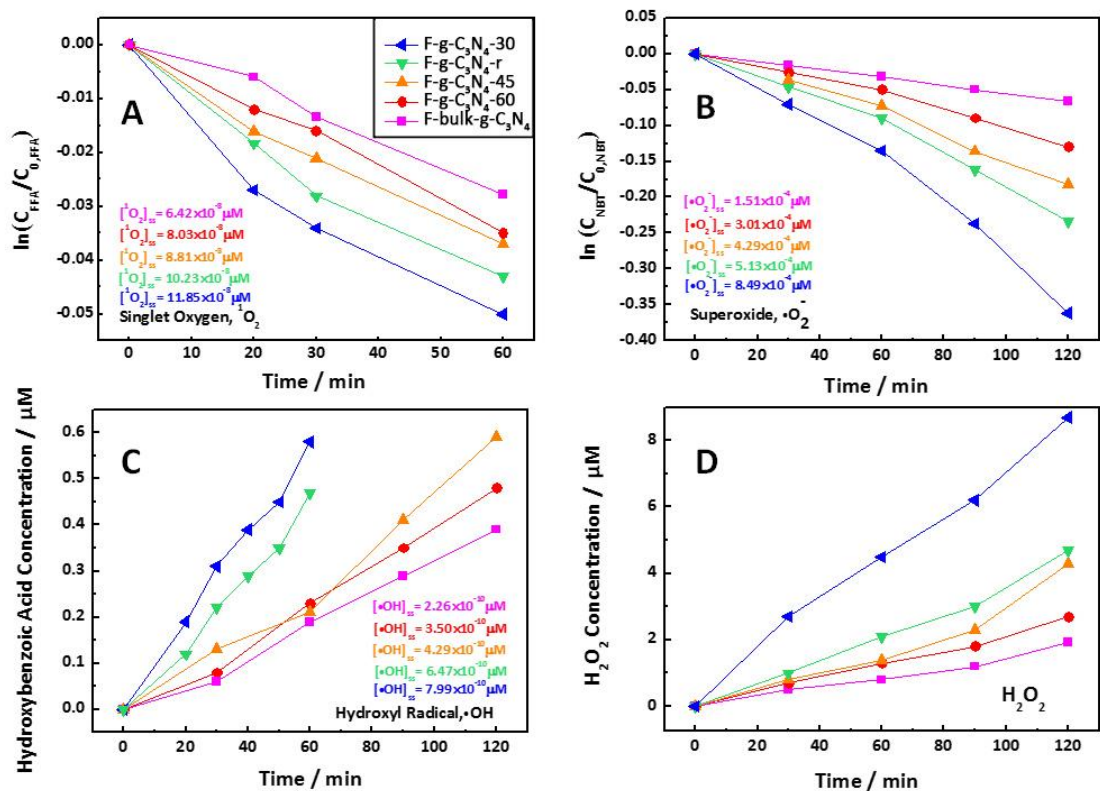


Figure S15. Measurements of steady state ROS concentration in the bulk solution. (A) Steady state concentration of 1O_2 calculated from the decreasing concentration of furfuryl alcohol. **(B)** Steady state concentration of $\cdot O_2^-$ calculated from the decreasing concentration of nitroblue tetrazolium. **(C)** Steady state concentration of $\cdot OH$ calculated from the increasing concentration of hydroxybenzoic acid. **(D)** Measurement of H_2O_2 concentration over the time.

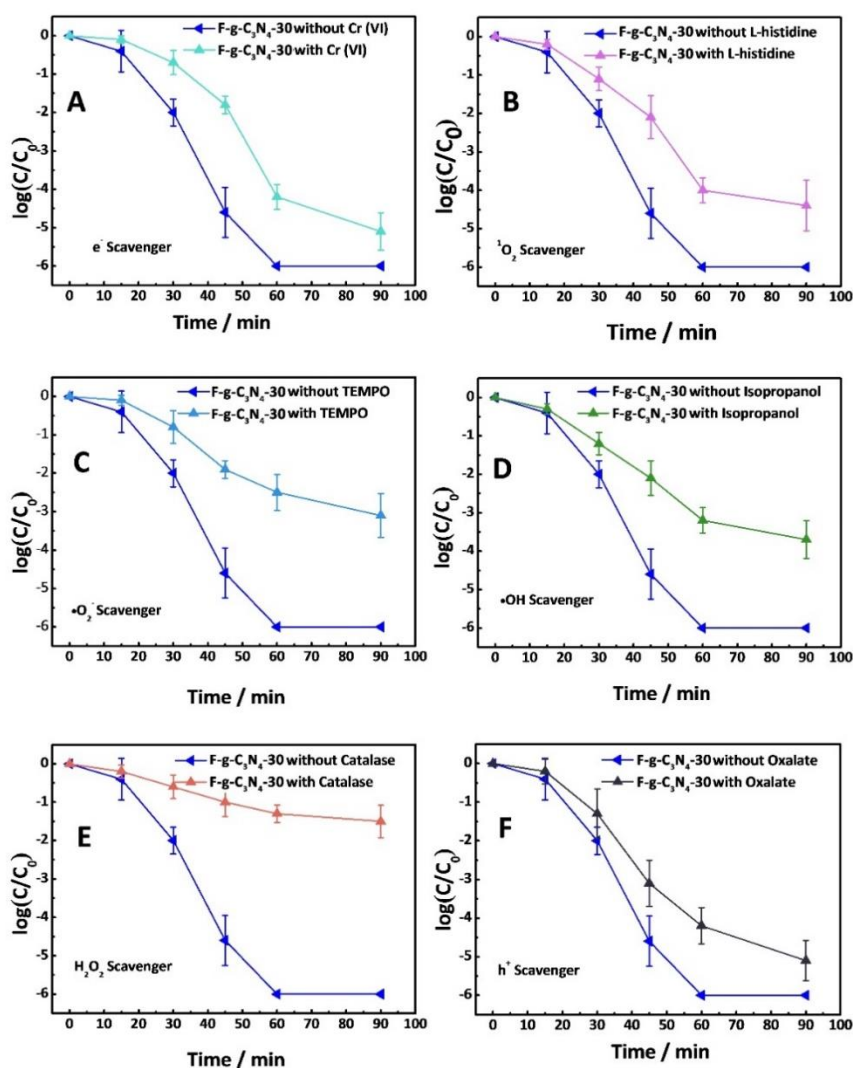


Figure S16. Photocatalytic scavenger quenching experiments using F-g-C₃N₄-30 as the catalyst. (A) Disinfection performance using Cr (VI) to quench photo-generated e⁻. (B) Disinfection performance using L-histidine to quench photo-generated ¹O₂. (C) Disinfection performance using TEMPO to quench photo-generated ·O₂⁻. (D) Disinfection performance using scavenger isopropanol to quench photo-generated ·OH. (E) Disinfection performance using catalase to quench photo-generated H₂O₂. (F) Disinfection performance using sodium oxalate to quench photo-generated h⁺. In these disinfection performance curves, error bars represent the standard deviation of five replicate measurements.

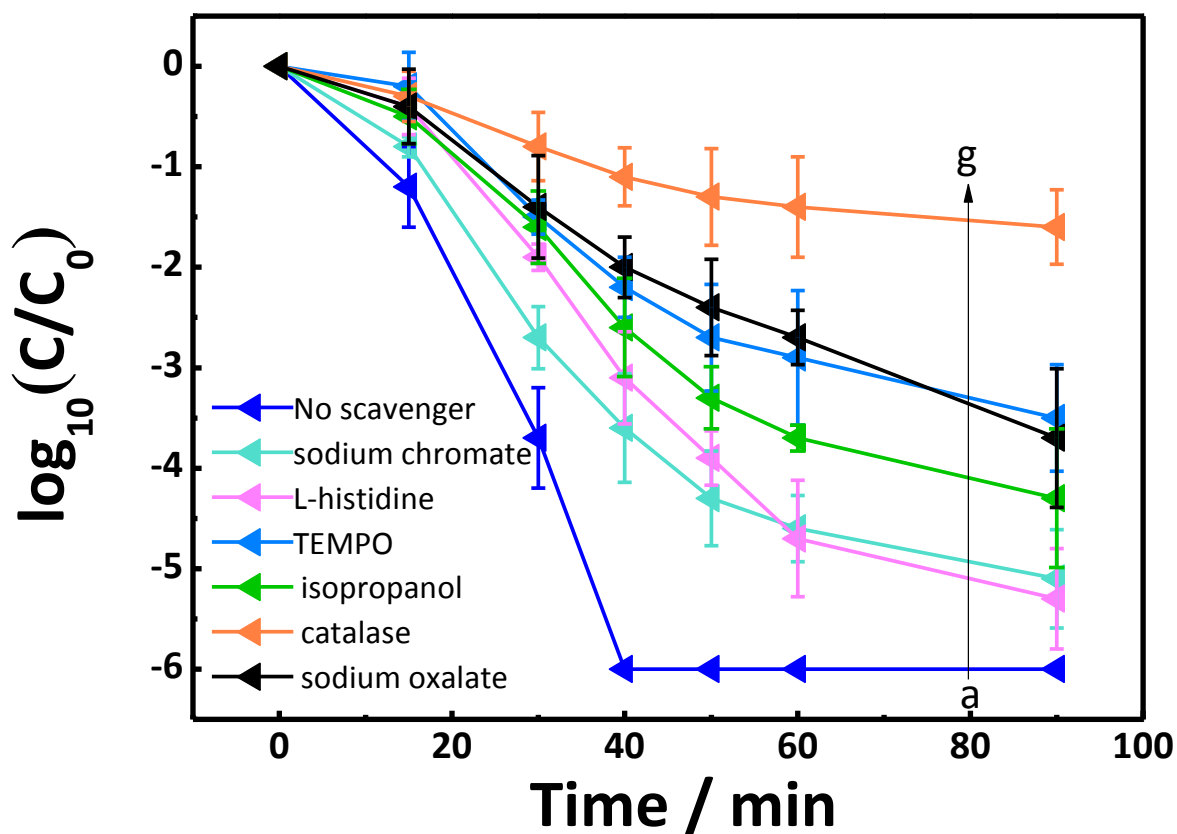


Figure S17. Scavengers quenching experiments of g-C₃N₄-30 suspension (The concentration of g-C₃N₄-30 is 10 mg/L). Colored lines represent the results of disinfection experiments conducted with the presence of different scavengers. (From line a to line g: Photocatalytic disinfection performance of g-C₃N₄-30 in suspension without any scavenger (a), with sodium chromate for quenching e⁻ (b), with L-histidine for quenching ¹O₂ (c), isopropanol for quenching photo generated ·OH (d), with scavenger sodium oxalate for quenching photo generated h⁺ (e) with TEMPO for quenching ·O₂⁻ (f), with catalase for quenching H₂O₂ (g).) In the disinfection performances, error bars represent the standard deviation of five replicate measurements.

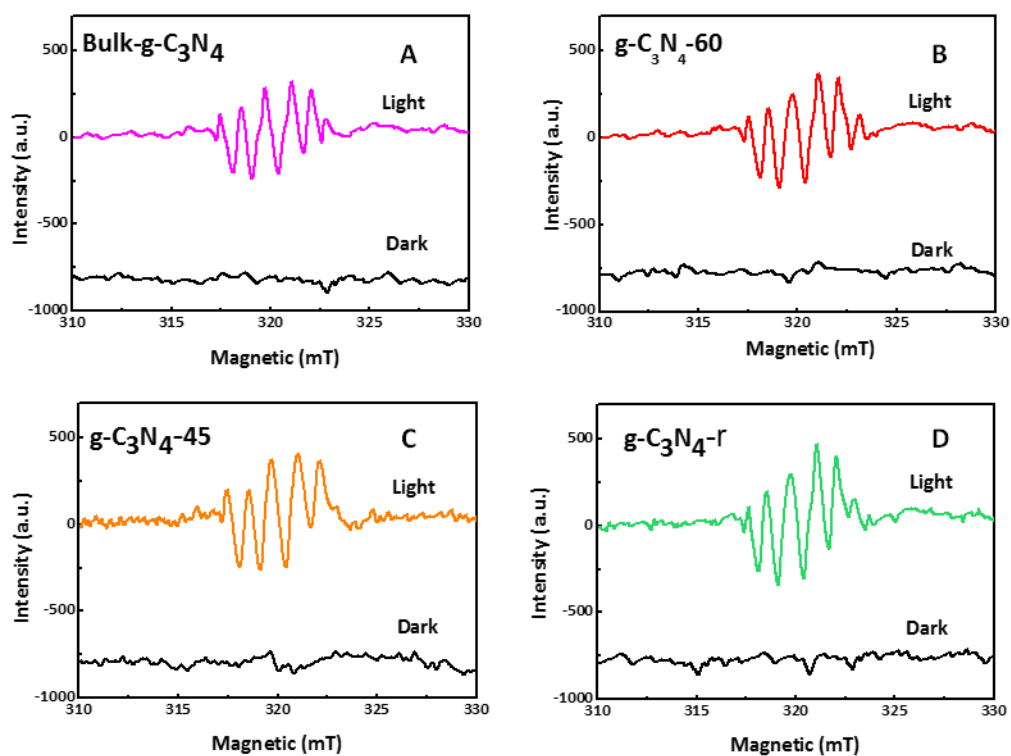


Figure S18. ESR spectra of different $g\text{-C}_3\text{N}_4$ samples. ESR spectra of (A) bulk- $g\text{-C}_3\text{N}_4$, (B) $g\text{-C}_3\text{N}_4\text{-60}$, (C) $g\text{-C}_3\text{N}_4\text{-45}$ and (D) $g\text{-C}_3\text{N}_4\text{-r}$ under visible-light illumination in methanol solution.

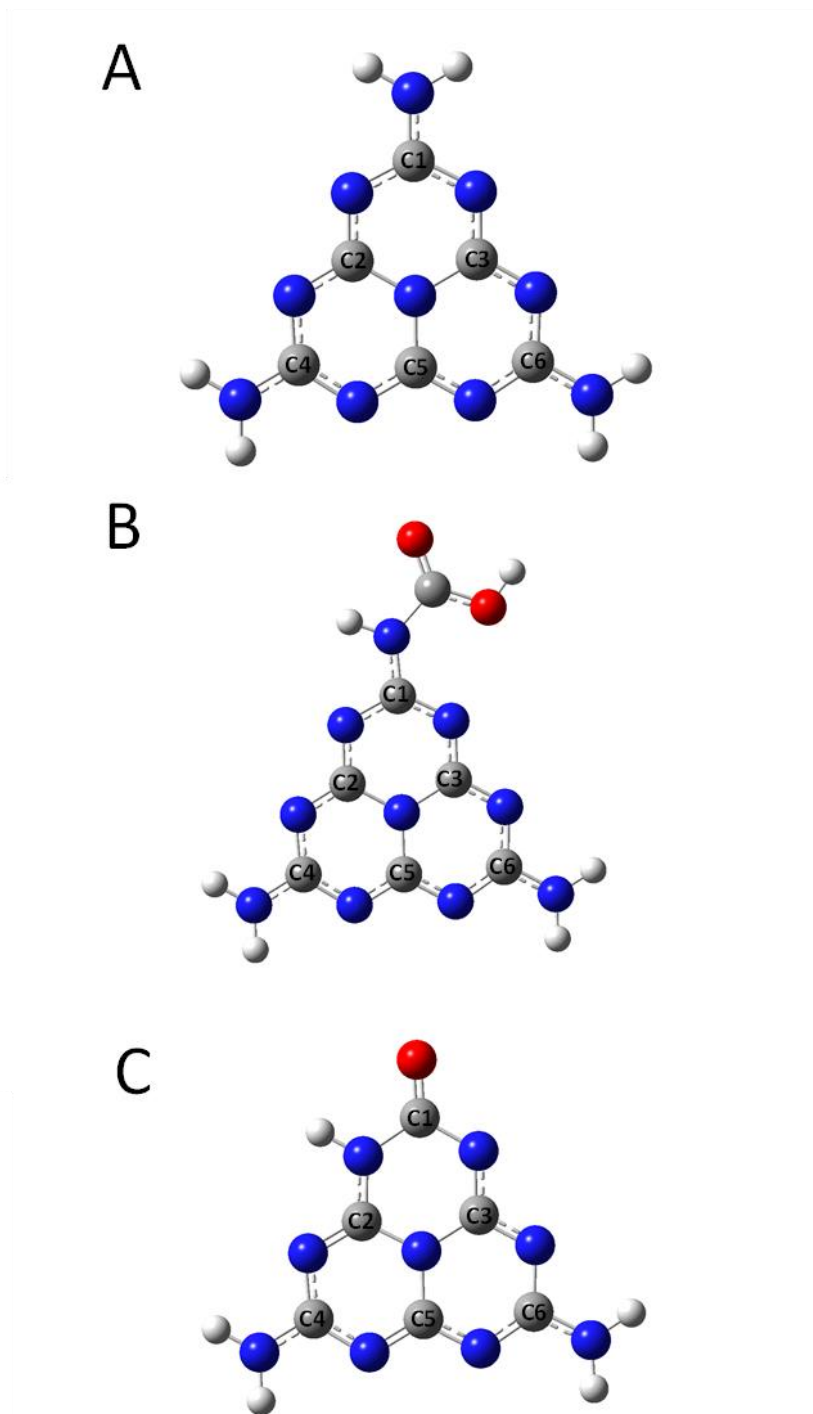


Figure S19. Diagram of the models for the DFT calculations. (A) M_{elem} (B) $M_{elem-OH}$ and (C) $M_{elem-COOH}$.

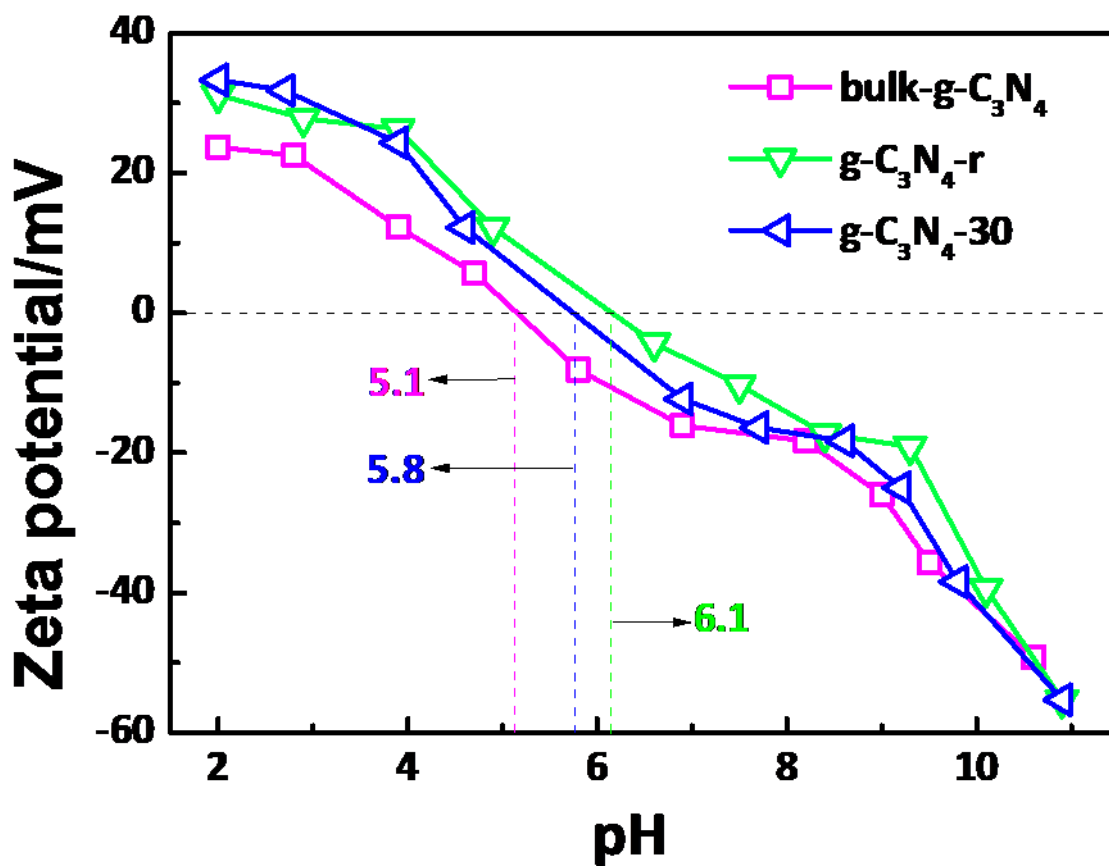


Figure S20. Zeta potentials of bulk-g-C₃N₄, g-C₃N₄-30, and g-C₃N₄-r as functions of the pH value of the suspensions. Each value of Zeta potential is the average value of three replicate measurements.

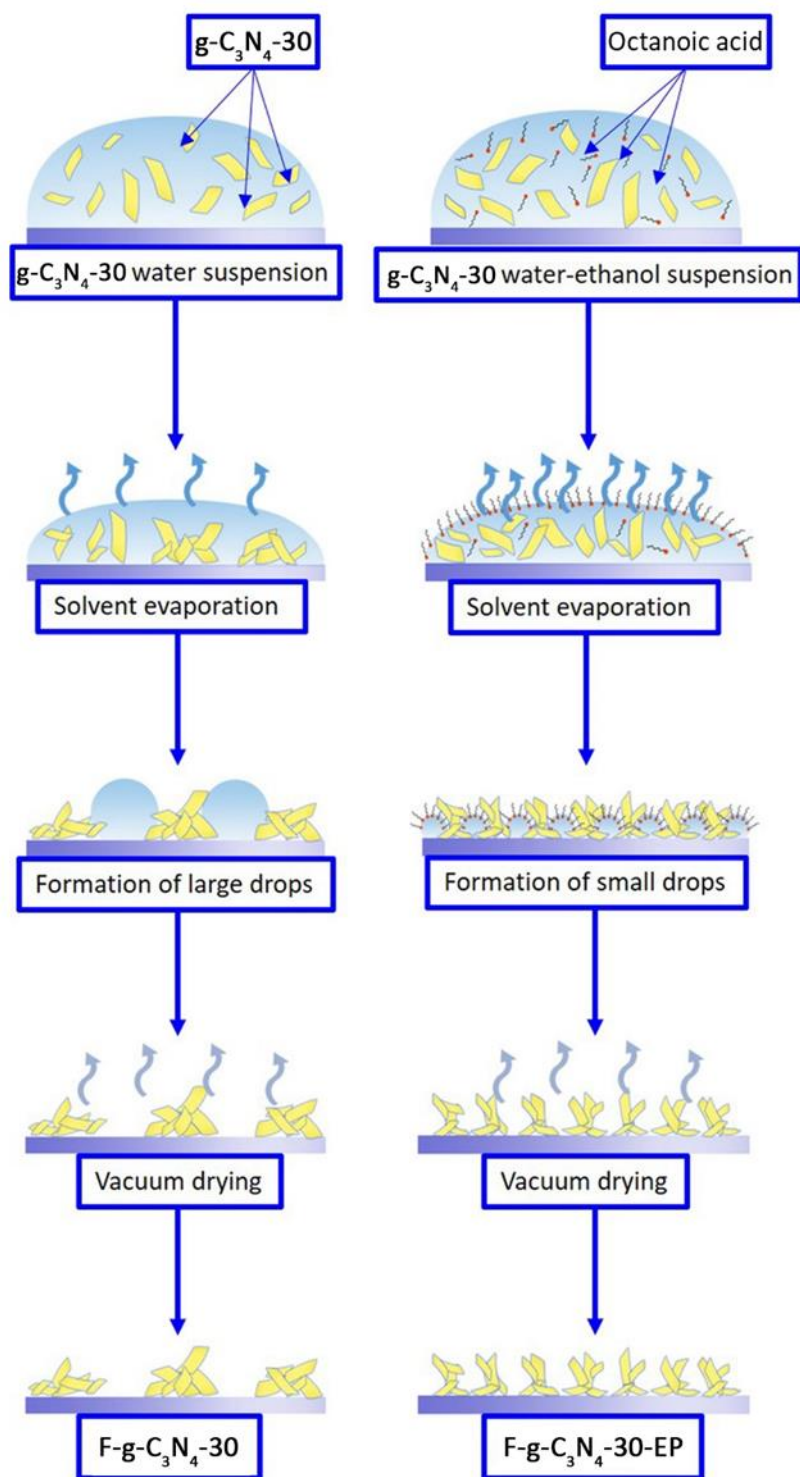


Figure S21. Systematic diagram of self-assembly strategies in different solvents.

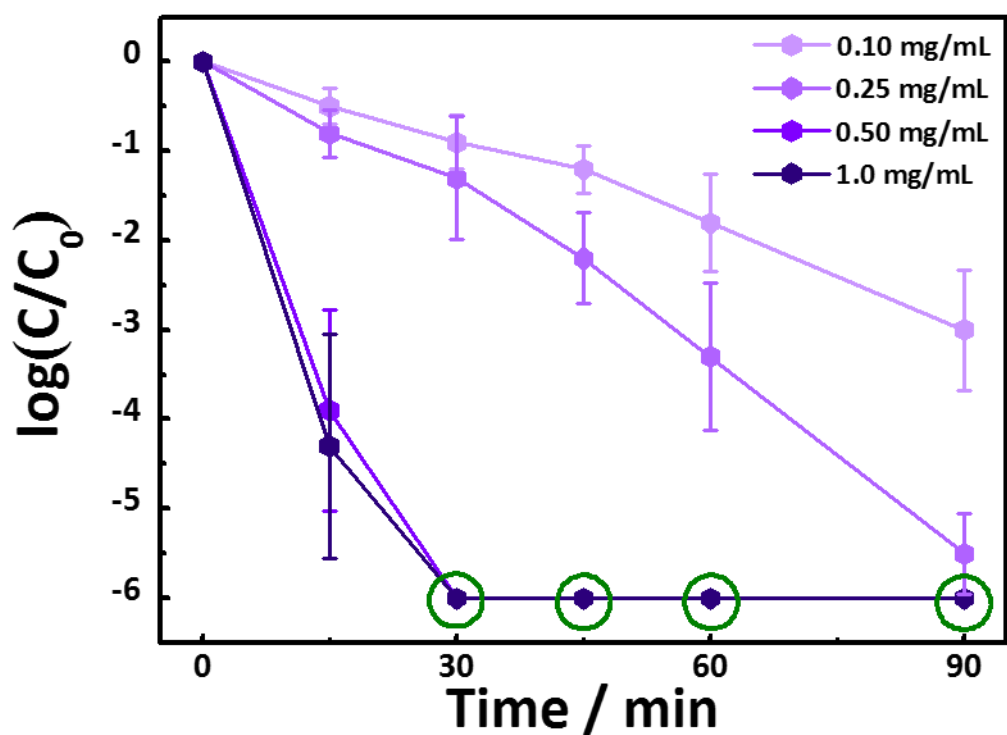


Figure S22. Optimization of modification mass of F-g-C₃N₄-30-EP. Photocatalytic disinfection performance using several F-g-C₃N₄-30-EP samples with different mass concentrations (the mass concentrations of the photocatalysts in 50 mL aqueous solution are indicated in the figure). The modification volume of the suspension is 1 mL.

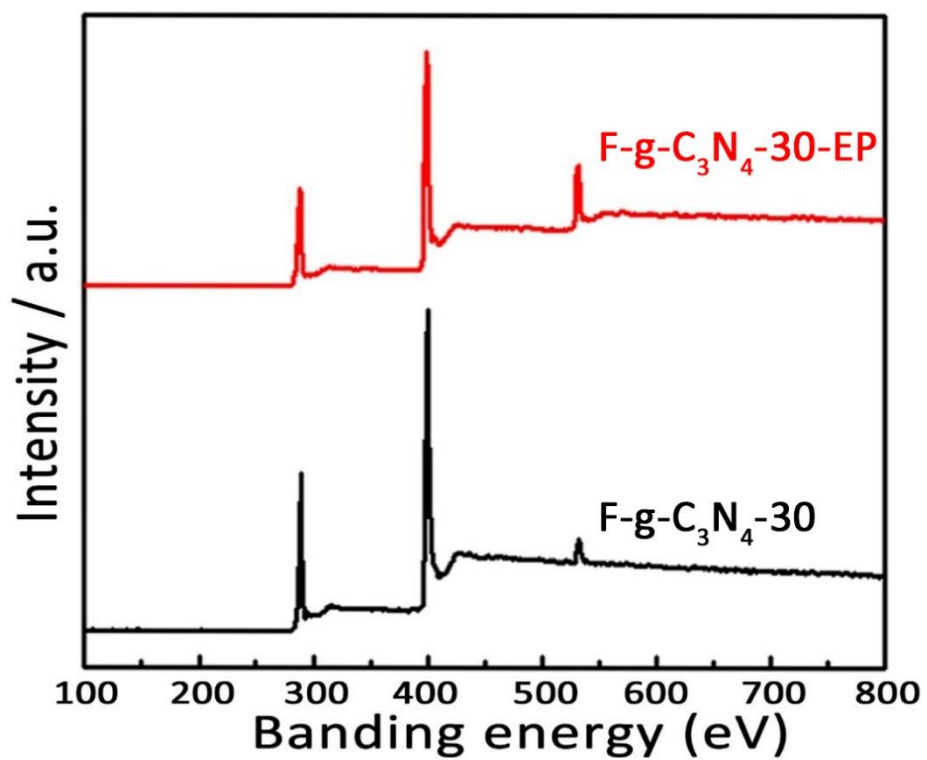


Figure S23. XPS survey spectra for F-g-C₃N₄-30-EP and F-g-C₃N₄-30.

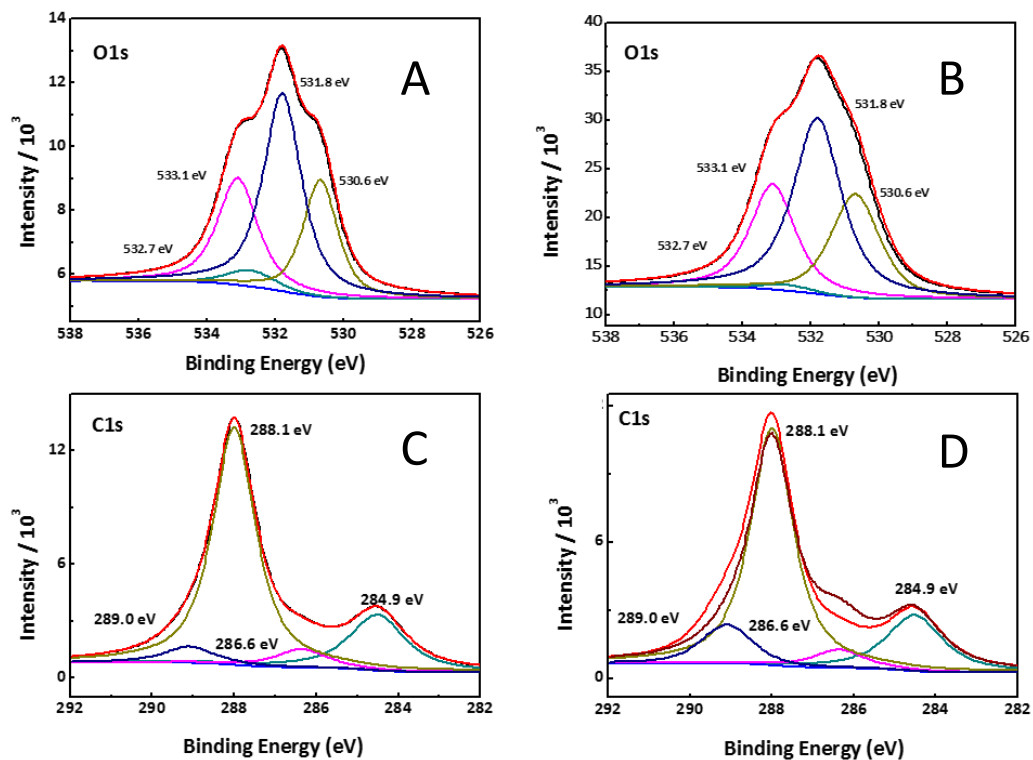


Figure S24. High-resolution XPS spectra O 1s of g-C₃N₄ samples. High-resolution XPS spectra O 1s of (A) F-g-C₃N₄-30 and (B) F-g-C₃N₄-30-EP. High-resolution C 1s spectra of (C) F-g-C₃N₄-30 and (D) F-g-C₃N₄-30-EP.

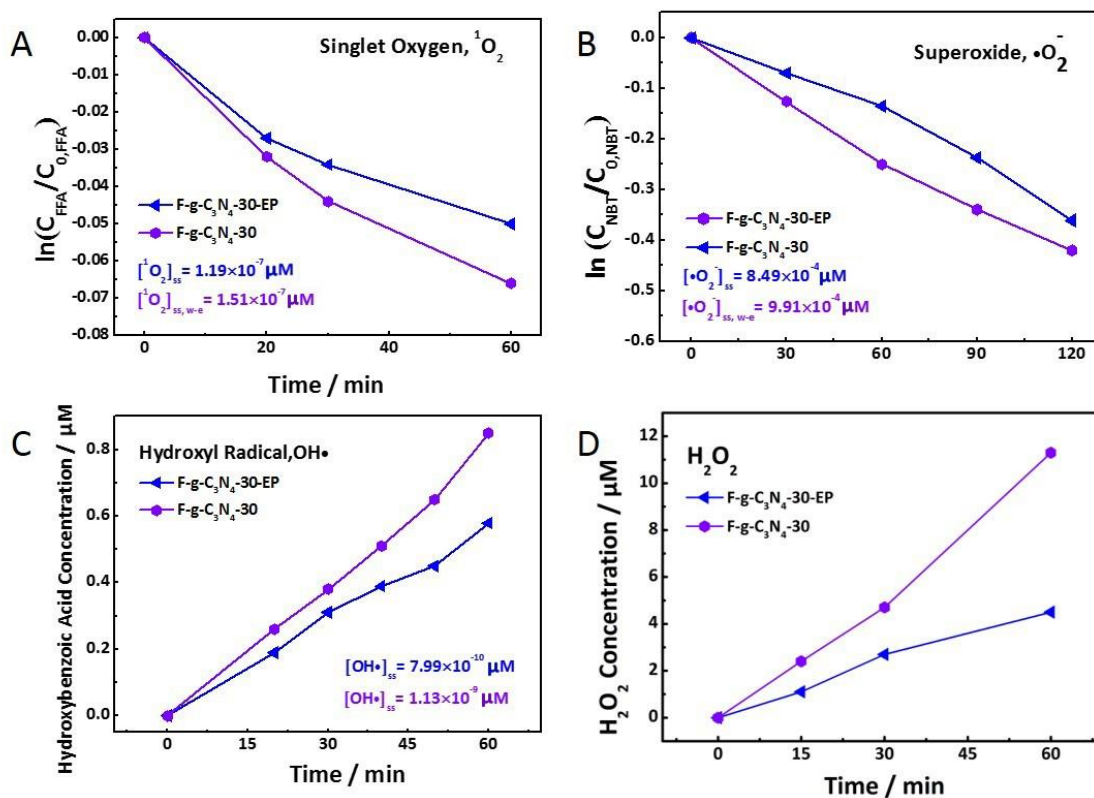


Figure S25. Comparison between ROS generation rate of F-g-C₃N₄-30 (blue lines) and F-g-C₃N₄-30-EP (purple lines). (A) Comparison of steady state concentration of $^1\text{O}_2$ calculated from the decreasing concentration of furfuryl alcohol. (B) Comparison of steady state concentration of $\cdot\text{O}_2^-$ calculated from the decreasing concentration of nitroblue tetrazolium. (C) Comparison of steady state concentration of $\cdot\text{OH}$ calculated from the increasing concentration of hydroxybenzoic acid. (D) Comparison of H_2O_2 concentration measured over the time.

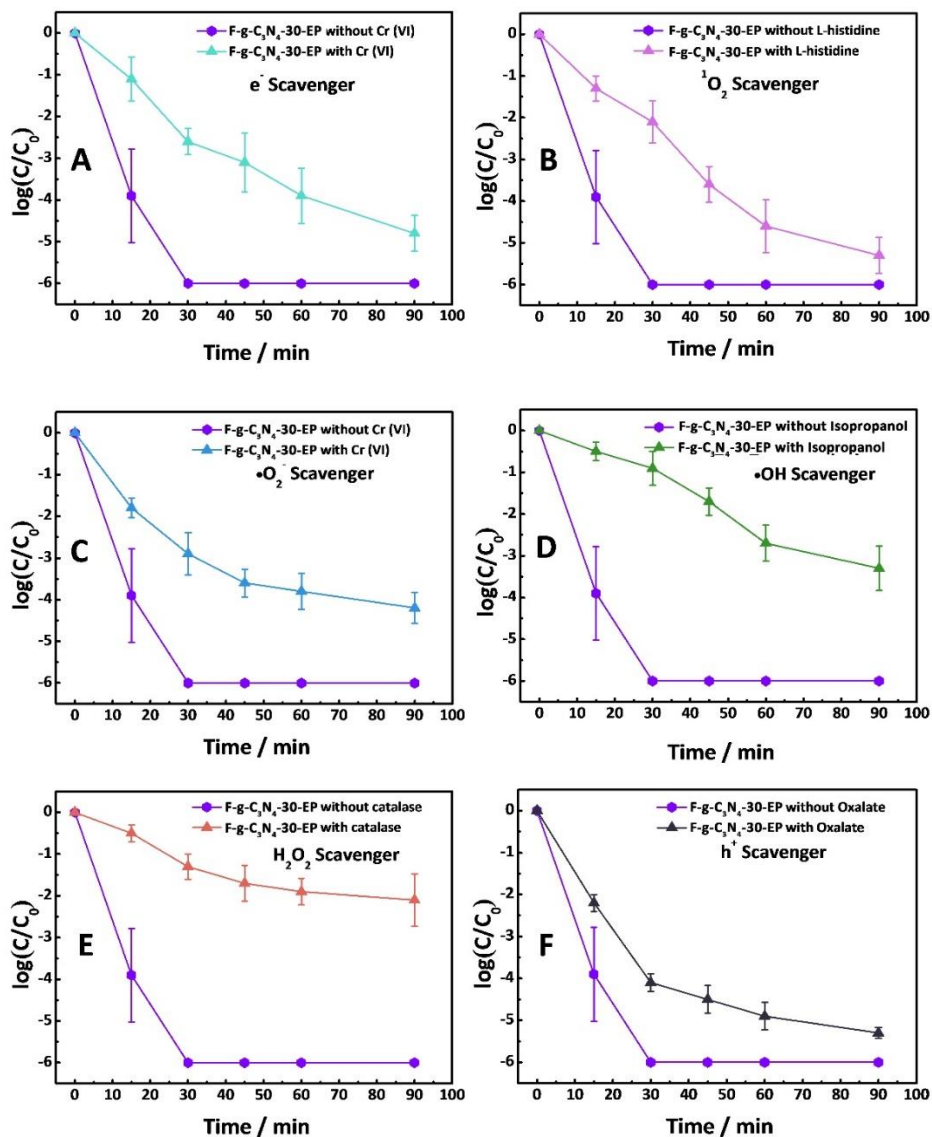


Figure S26. Photocatalytic scavenger quenching experiments with F-g-C₃N₄-30-EP. (A) Disinfection performance using Cr (VI) to quench photo-generated e^- . (B) Disinfection performance using L-histidine to quench photo-generated 1O_2 . (C) Disinfection performance using Cr (VI) to quench photo-generated $\cdot O_2^-$. (D) Disinfection performance using catalase to quench photo-generated H_2O_2 . (E) Disinfection performance using isopropanol to quench photo-generated $\cdot OH$. (F) Disinfection performance using sodium oxalate to quench photo-generated h^+ . In these disinfection performance curves, error bars represent the standard deviation of five replicate measurements.

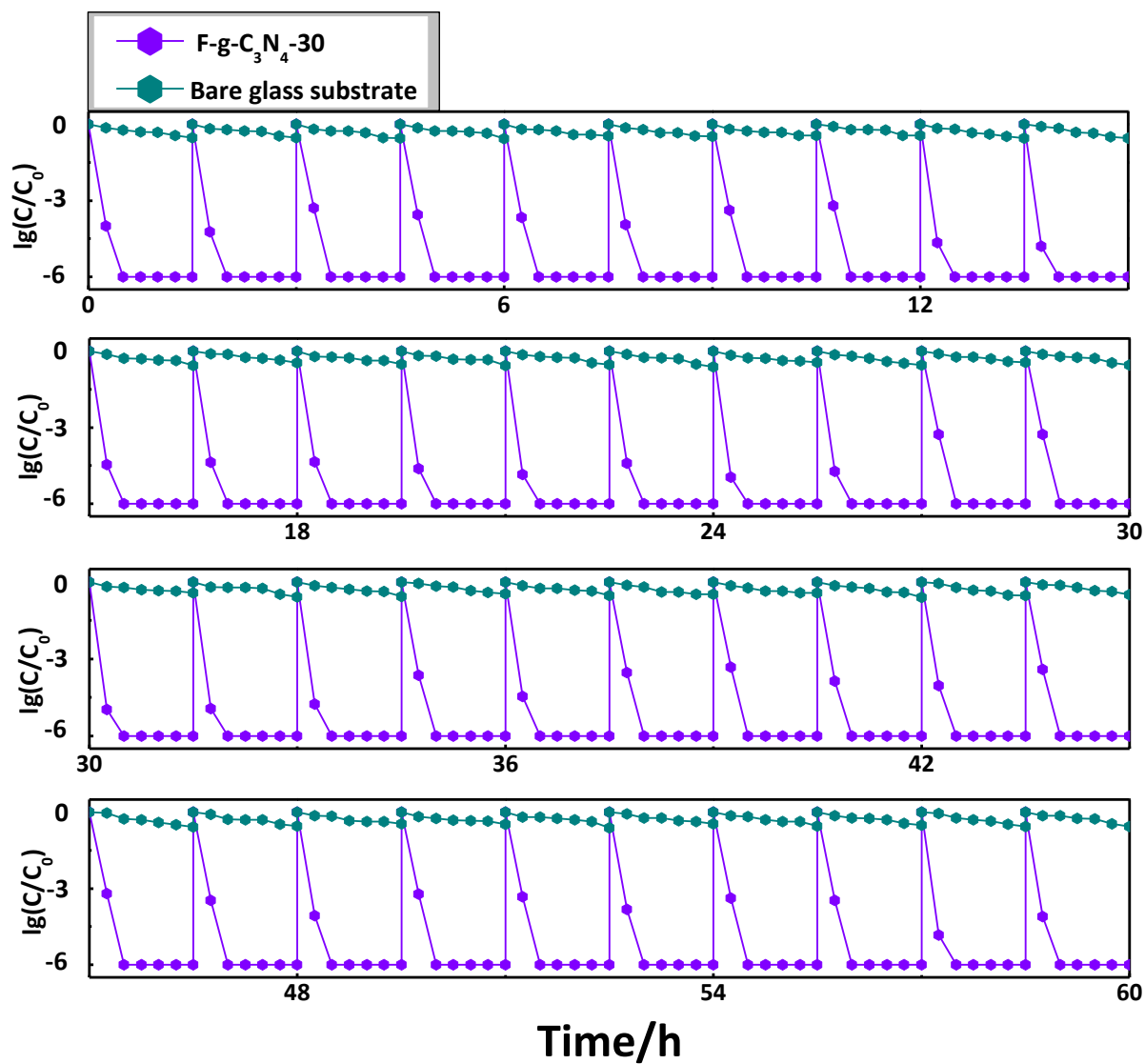


Figure S27. Stability of F-g-C₃N₄-30-EP. Photocatalytic disinfection performance of F-g-C₃N₄-30, which is used for 40 cycles (60 h) under visible light irradiation. After each disinfection circle, the fixed catalyst was washed by deionized water.

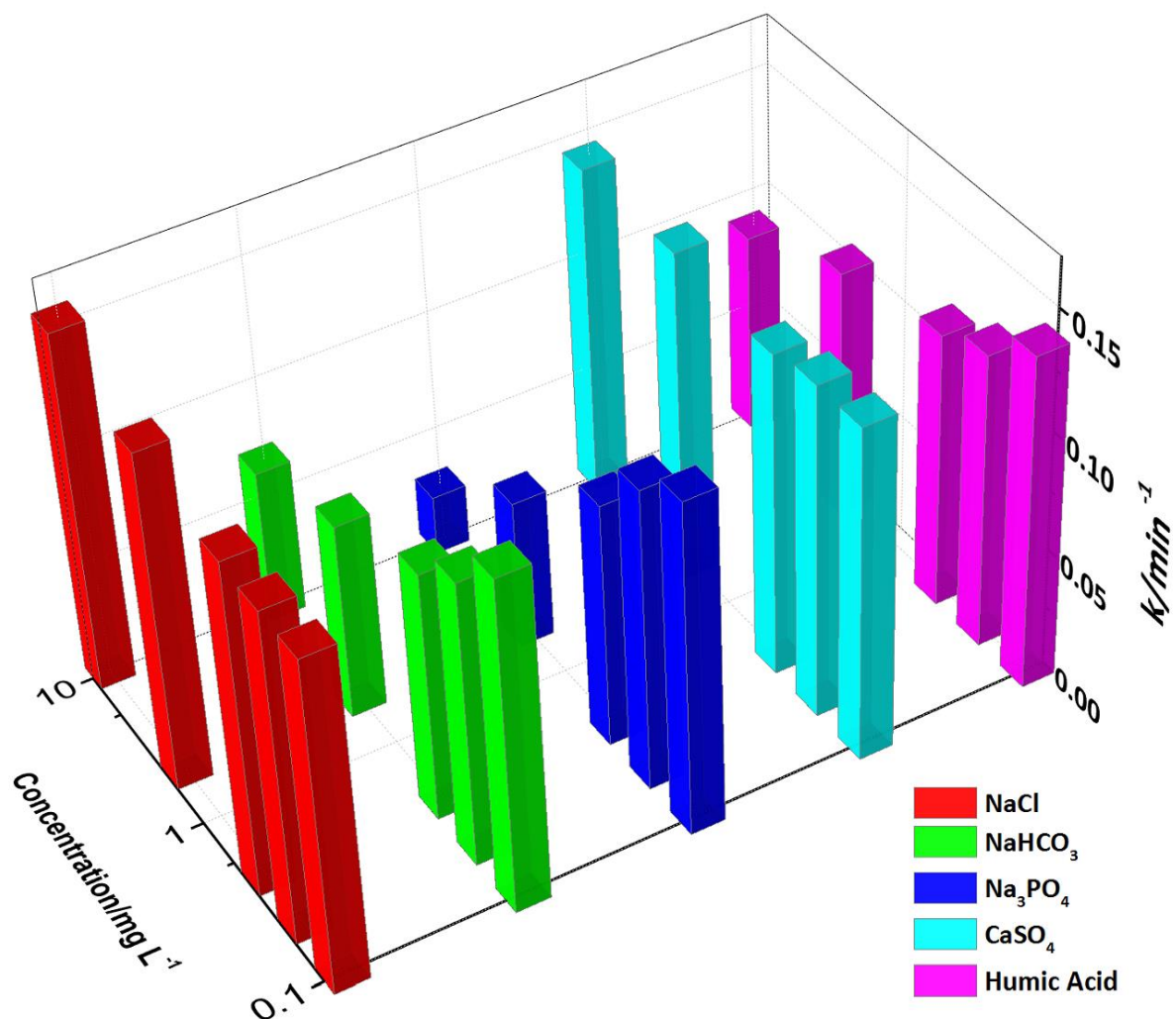


Figure S28. Inhibition and poisoning of catalyst caused by common substances in environmental water. k is the first-order disinfection rate of F-g-C₃N₄-EP after addition of common substance in environmental water.

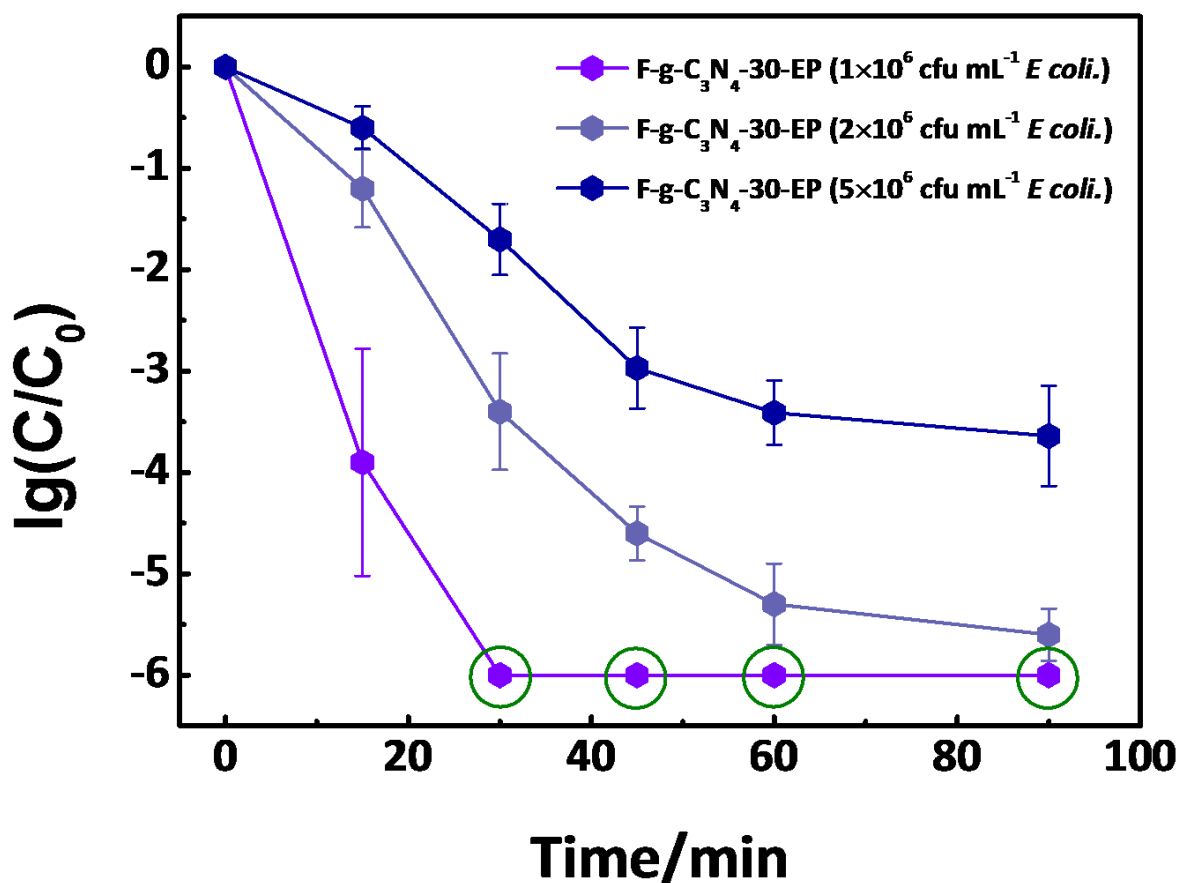


Figure S29. Solid-poisoning effects of F-g-C₃N₄-30-EP. Photocatalytic disinfection measurements of F-g-C₃N₄-EP in *E. coli.* suspension of different concentrations. In the disinfection performance curves, error bars represent the standard deviation of five replicate measurements and the data point with dark green circle means that no live bacterium was detected. Tests conducted under visible light was simulated by a xenon lamp with a long-pass filter ($\lambda > 400$ nm).

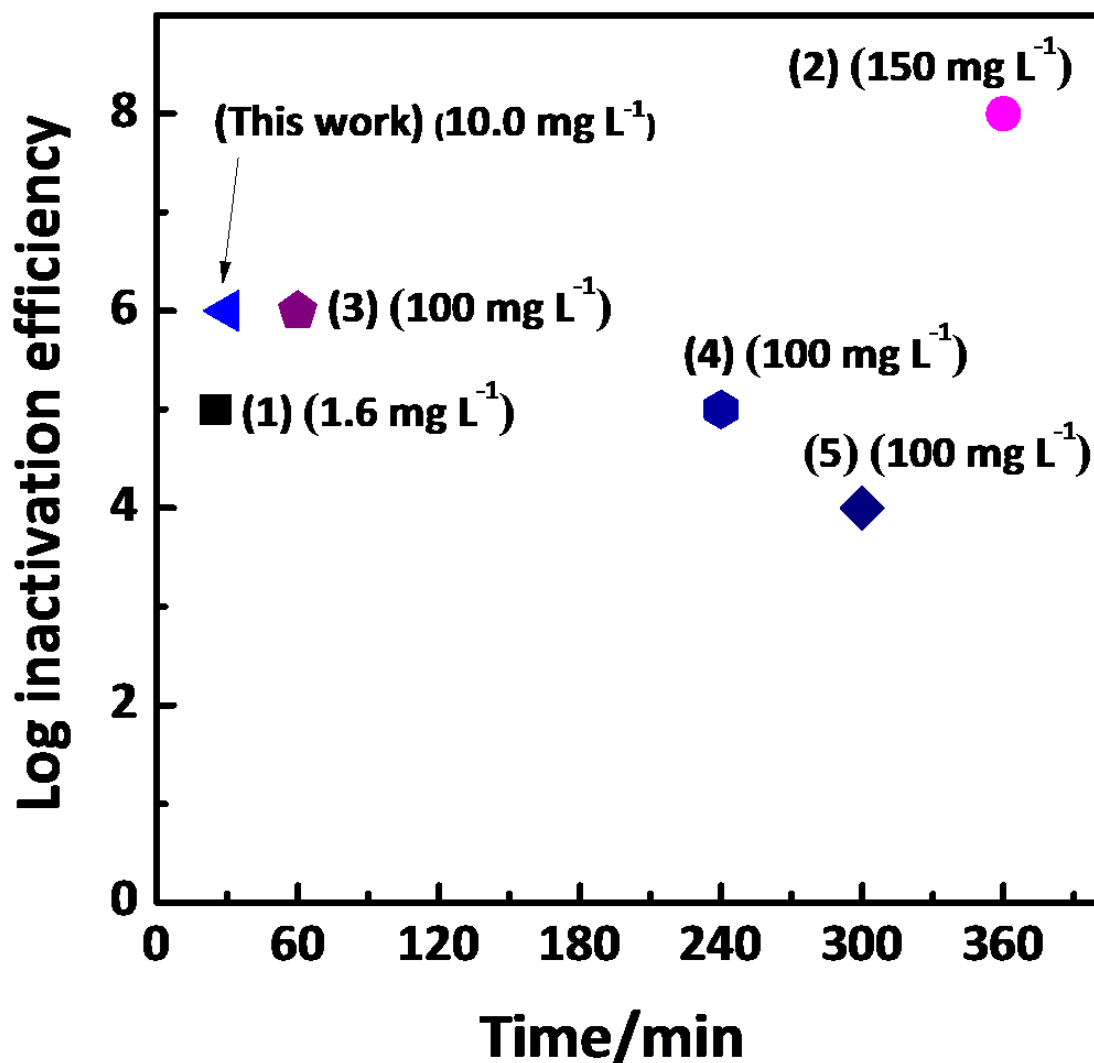


Figure S30. Comparison of log disinfection performance (utilization mass, disinfection efficiency and disinfection capability) of F-g-C₃N₄-30-EP with the efficiency of other photocatalysts: F-g-C₃N₄-30-EP (this work, 5 cm² equivalent to 10.0 mg L⁻¹), (1) Cu-MoS₂ (1.6 mg/L, 100 mW/cm², ref. 13), (2) Bulk g-C₃N₄ (150 mg/L, 150 mW/cm², ref. 35, for MS2 inactivation), (3) GO-CdS (100 mg/L, 100 mW/cm², ref. 37), (4) S-GO-C₃N₄ (100 mg/L, 193 mW/cm², ref. 33) and (5) Single layer C₃N₄ (100 mg/L, 100 mW/cm², ref. 32). The number of ref. refers to the number of ref. in the manuscript.

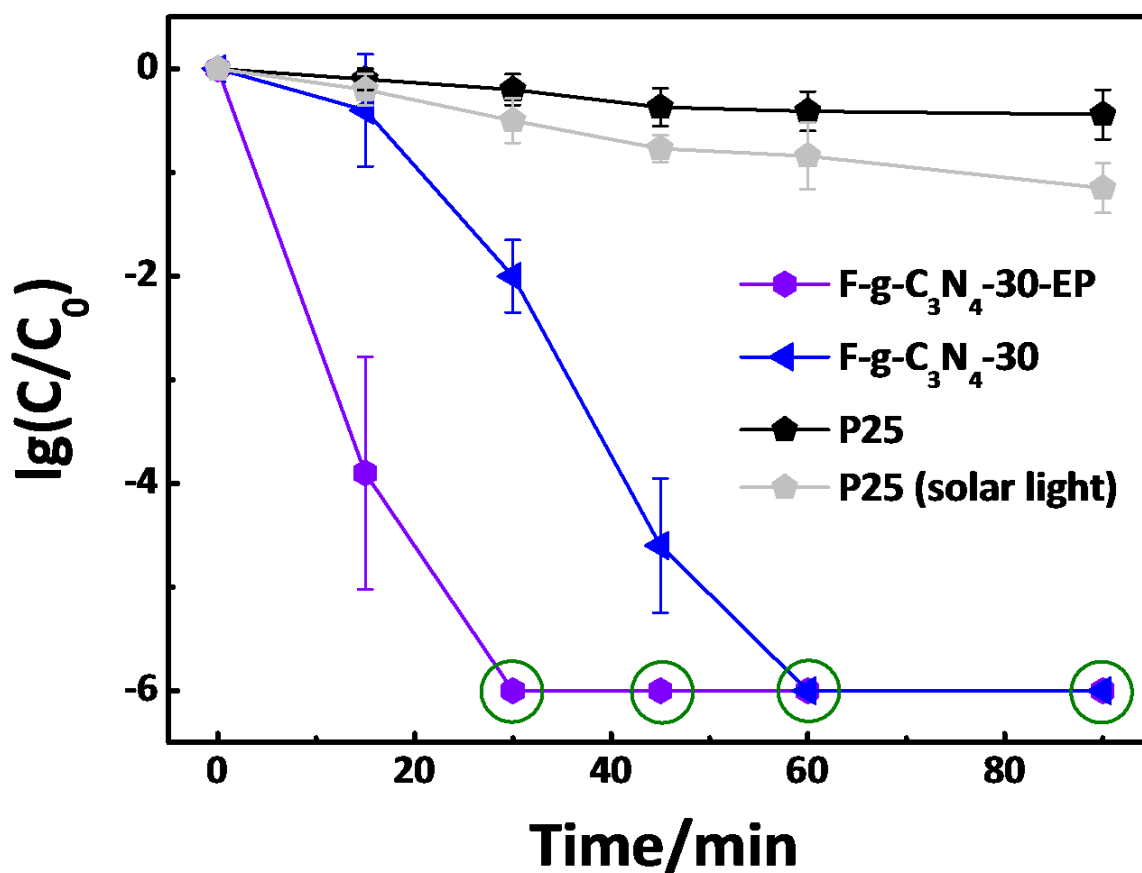


Figure S31. Comparison of log disinfection performance of F-g-C₃N₄-30-EP and F-g-C₃N₄-30 under visible light with that of P25 modified glass substrate (2 cm × 2.5 cm) under visible or solar light. The catalyst concentration of P25 in the system is the same as that of g-C₃N₄-30 (10 mg/L). In the disinfection performance curves, error bars represent the standard deviation of five replicate measurements and the data point with dark green circle means that no live bacterium was detected. Tests conducted under visible light was simulated by a xenon lamp with a long-pass filter ($\lambda > 400$ nm, light intensity is 100 mW/cm²); Tests conducted under solar light was simulated by the xenon lamp without the long-pass filter.

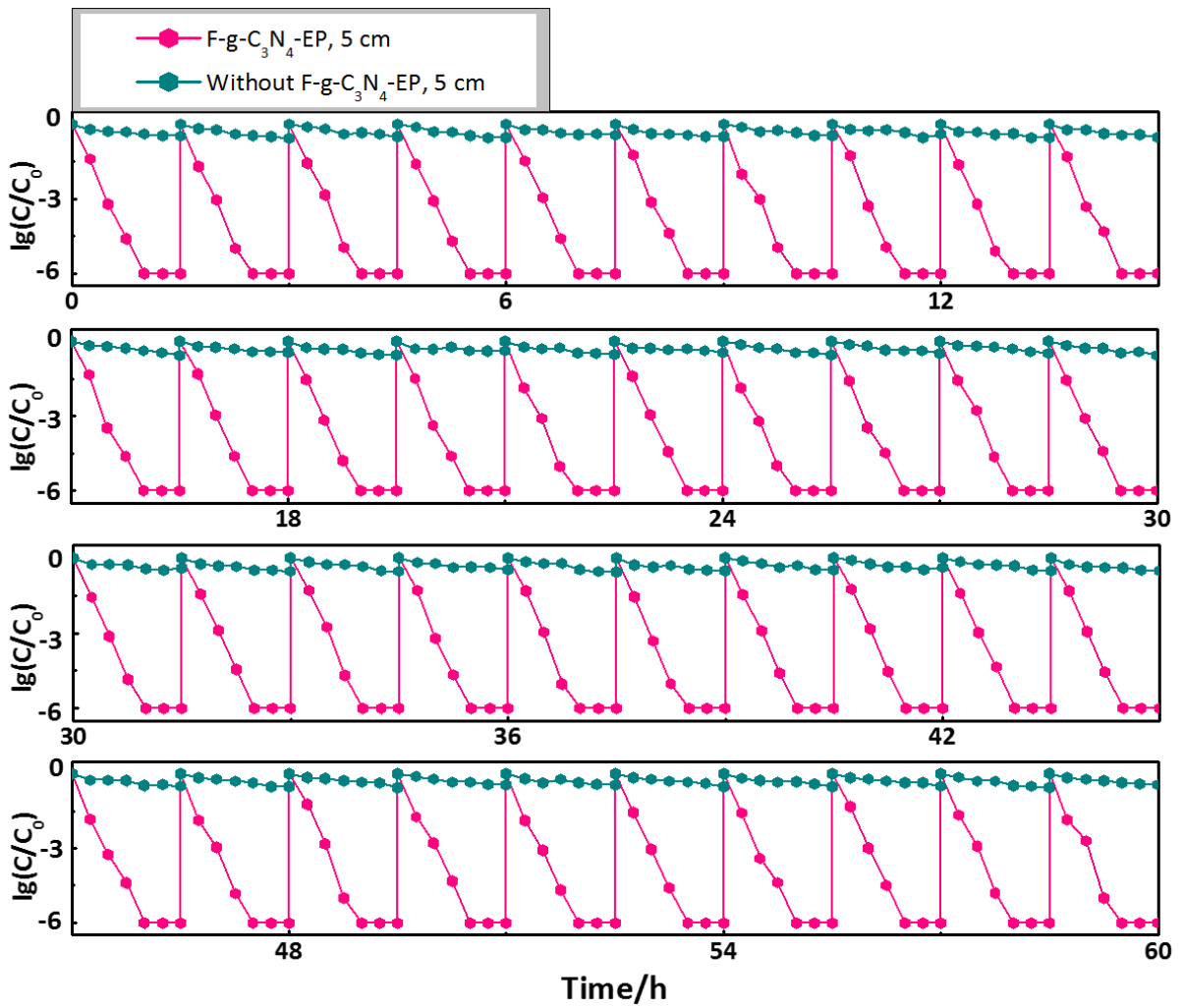


Figure S32. Long-term measurements (60 h, 40 cycles) of the $F-g-C_3N_4-30-EP$ modified plastic bags in disinfection experiments. After each 1.5 h disinfection process, the water in this bag was poured out, and the bag was washed by deionized water. Then, the bio-contaminated water containing *E. coli*. K-12 was immediately poured into the bag. The highest water depth in this bag was controlled to be 5 cm.

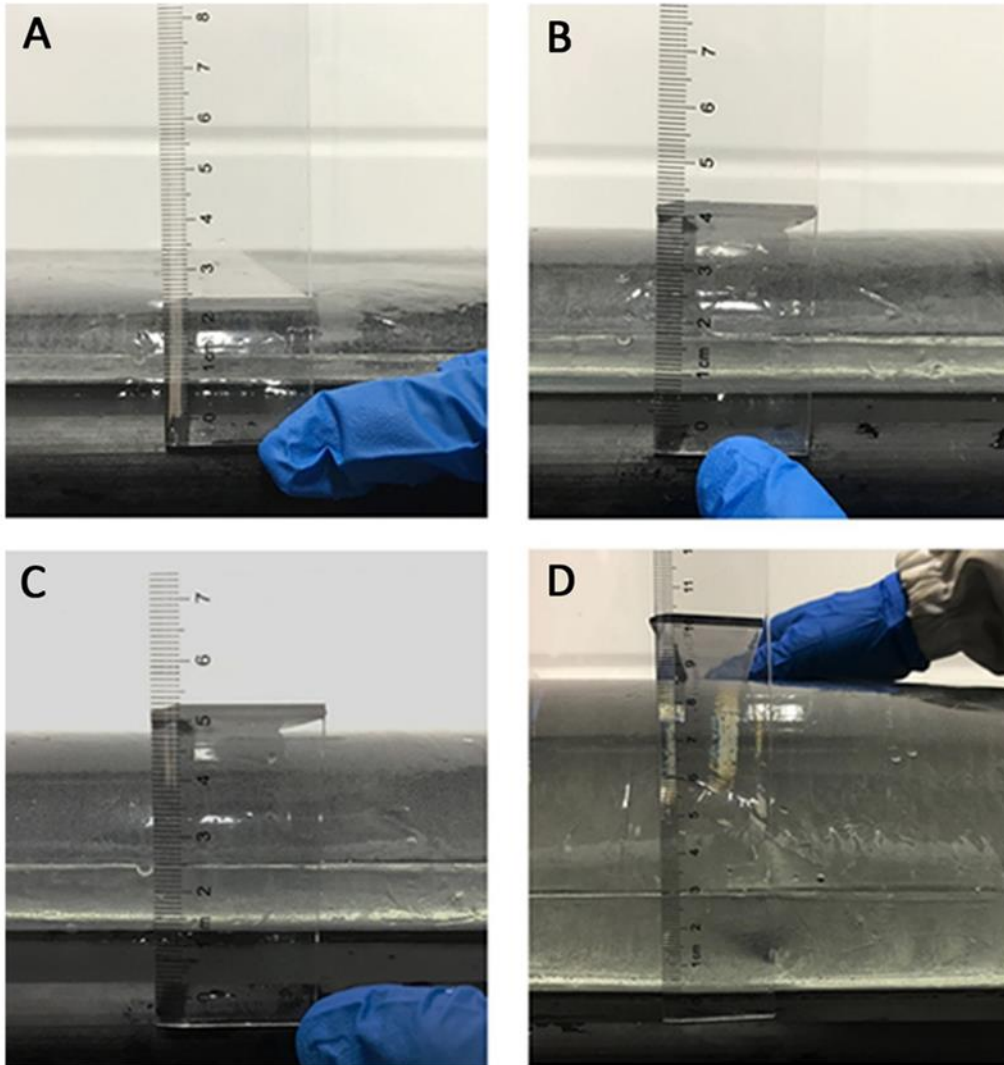


Figure S33. Investigation on the effect of different water depths on the disinfection performance when treating contaminated water: (A) 2 cm, (B) 4 cm, (C) 5 cm and (D) 10 cm.

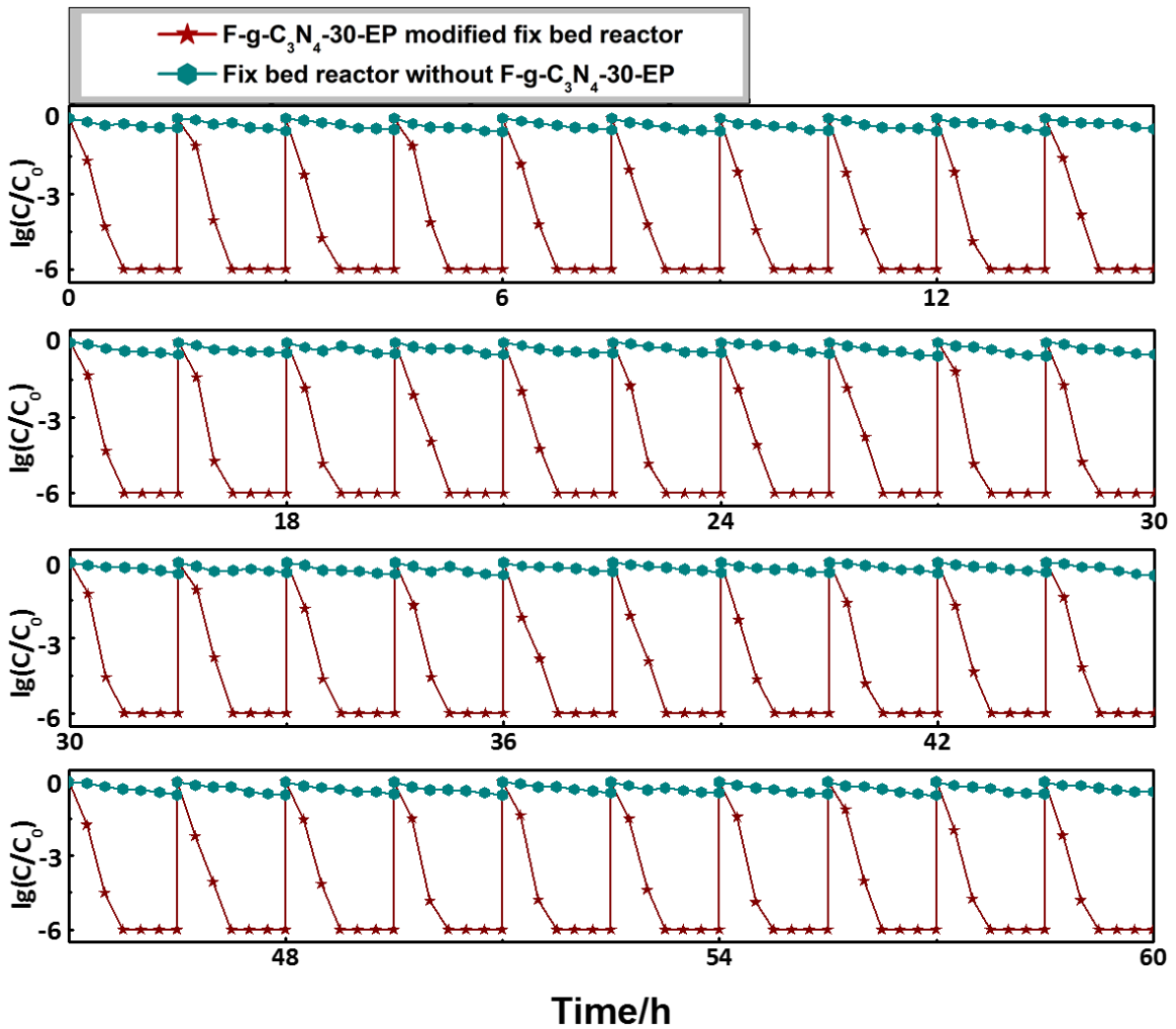


Figure S34. Long-term measurements (60 h, 40 cycles) of the F-g-C₃N₄-30-EP modified fix bed reactor in disinfection experiments. After each 1.5 h disinfection process, the water in this reactor was pumped out, and the bag was washed by deionized water. Then, the bio-contaminated water containing *E. coli*. K-12 was immediately pumped into the reactor. When the bio-contaminated water quickly filled up the reactor with water depth of 2 cm, the flowing rate of the water was 3 mL/min.

Table S1. Integral area ratios of the main peaks of O 1s and C 1s in XPS spectra of g-C₃N₄ samples.

Sample name	Integral area of peak (mathematic)					C 1s Total	Integral area ratios (Area _{TotalO 1s} / Area _{TotalC 1s})
	Total	C-O	O 1s C=O	COOH	H ₂ O		
bulk-g-C ₃ N ₄	0	0	0	0	0	150430	0
g-C ₃ N ₄ -r	2450	547	849	1054	0	148026	0.017
g-C ₃ N ₄ -30	13016	2414	5418	4443	741	129795	0.10
g-C ₃ N ₄ -45	41136	28926	5631	4626	1953	128549	0.32
g-C ₃ N ₄ -60	90012	77591	5685	4674	2062	126778	0.71

References:

[S1] Zheng, Y., Jiao, Y., Chen, J., Liu, J., Liang, J., Du, A., Zhang, W., Zhu, Z., Smith, S. C., Jaroniec, M., Lu, G.Q., and Qiao, S. Z. (2011). Nanoporous graphitic-C₃N₄@carbon metal-free electrocatalysts for highly efficient oxygen reduction. *J. Am. Chem. Soc.* *133*, 20116-20119.

[S2] Frisch, M. J., Trucks, G. W., Schlegel, H. B., Scuseria, G. E., Robb, M. A., Cheeseman, J. R., Scalmani, G., Barone, V., Mennucci, B., Petersson, G. A., Nakatsuji, H., Caricato, M., Li, X., Hratchian, H. P., Izmaylov, A. F., Bloino, J., Zheng, G., Sonnenberg, J. L., Hada, M., Ehara, M., Toyota, K., Fukuda, R., Hasegawa, J., Ishida, M., Nakajima, T., Honda, Y., Kitao, O., Nakai, H., Vreven, T., Montgomery Jr., J. A., Peralta, J. E., Ogliaro, F., Bearpark, M. J., Heyd, J., Brothers, E. N., Kudin, K. N., Staroverov, V. N., Kobayashi, R., Normand, J., Raghavachari, K., Rendell, A. P., Burant, J. C., Iyengar, S. S., Tomasi, J., Cossi, M., Rega, N., Millam, N. J., Klene, M., Knox, J. E., Cross, J. B., Bakken, V., Adamo, C., Jaramillo, J., Gomperts, R., Stratmann, R. E., Yazyev, O., Austin, A. J., Cammi, R., Pomelli, C., Ochterski, J. W., Martin, R. L., Morokuma, K., Zakrzewski, V. G., Voth, G. A., Salvador, P., Dannenberg, J. J., Dapprich, S., Daniels, A. D., Farkas, Ö., Foresman, J. B., Ortiz, J. V., Cioslowski, J. & Fox, D. J. *Gaussian 09*, Gaussian, Inc., Wallingford, CT, USA, 2009.